POLITECNICO DI TORINO
Repository ISTITUZIONALE

Flow dynamics and wall-pressure signatures in a high-Reynolds-number overexpanded nozzle with free shock separation

Original
Flow dynamics and wall-pressure signatures in a high-Reynolds-number overexpanded nozzle with free shock separation / Martelli, E., Saccoccio, L., Ciottoli, P.P., Tinney, C.E., Baars, W.J., Bernardini, M.. - In: JOURNAL OF FLUID MECHANICS. - ISSN 0022-1120. - 895:(2020). [10.1017/jfm.2020.280]

Availability:
This version is available at: 11583/2979602 since: 2025-02-05T11:55:53Z

Publisher:
Cambridge University Press

Published
DOI:10.1017/jfm.2020.280

Terms of use:

This article is made available under terms and conditions as specified in the corresponding bibliographic description in the repository

Publisher copyright

(Article begins on next page)

05 September 2026

J. Fluid Mech. (2020), *vol.* 895, A29. © The Author(s), 2020.
Published by Cambridge University Press
doi:10.1017/jfm.2020.280

Flow dynamics and wall-pressure signatures in a high-Reynolds-number overexpanded nozzle with free shock separation

E. Martelli[1], L. Saccoccio[2], P. P. Ciottoli[2], C. E. Tinney[3], W. J. Baars[4] and M. Bernardini[2,†]

[1]Dipartimento di Ingegneria, Università degli Studi della Campania 'L. Vanvitelli', 81100 Caserta, Italy

[2]Dipartimento di Ingegneria Meccanica e Aerospaziale, Sapienza Università di Roma, 00184 Roma, Italy

[3]Applied Research Laboratories, University of Texas at Austin, Austin, TX 78713, USA

[4]Faculty of Aerospace Engineering, Delft University of Technology, 2629 HS Delft, The Netherlands

(Received 17 June 2019; revised 25 March 2020; accepted 5 April 2020)

A delayed detached eddy simulation of an overexpanded nozzle flow with shock-induced separation is carried out at a Reynolds number of 1.7×10^7, based on nozzle throat diameter and stagnation chamber properties. In this flow, self-sustained shock oscillations induce local unsteady loads on the nozzle wall as well as global off-axis forces. Despite several studies in the last few decades, a clear physical understanding of the factors driving this unsteadiness is still lacking. The geometry under investigation is a subscale truncated ideal contour nozzle, which was experimentally tested at the University of Texas at Austin at a nozzle pressure ratio of 30. Under these conditions, the nozzle operates in a highly overexpanded state and comprises a conical separation shock that merges to form a Mach disk at the nozzle centre. The delayed detached eddy simulation model agrees well with the experimental results in terms of mean and fluctuating wall-pressure statistics. Wall-pressure spectra reveal a large bump at low frequencies associated with an axisymmetric (piston-like) motion of the shock system, followed by a broad and high-amplitude peak at higher frequencies associated with the Mach waves produced by turbulent eddies convecting through the detached shear layer. Moreover, a distinct peak at an intermediate frequency ($\sim$1 kHz) persists in the wall-pressure spectra downstream of the separation shock. A Fourier-based analysis performed in both time and space (azimuthal wavenumber) reveals that this intermediate-frequency peak is associated with the $m = 1$ (non-symmetric) pressure mode and is thus related to the generation of aerodynamic side loads. It is then shown how the unsteady Mach disk motion is characterized by an intense vortex shedding activity that, together with the vortical structures of the annular shear layer, contributes to the sustainment of an aeroacoustic feedback loop occurring within the nozzle.

Key words: compressible turbulence, jets, shock waves

† Email address for correspondence: matteo.bernardini@uniroma1.it

Downloaded from https://www.cambridge.org/core. IP address: 151.24.234.247, on 27 May 2020 at 05:31:14, subject to the Cambridge Core terms of use, available at https://www.cambridge.org/core/terms.
https://doi.org/10.1017/jfm.2020.280

1. Introduction

The performance of a first-stage liquid propellant rocket engine is highly dependent on the behaviour of the flow as it expands through a supersonic nozzle. Given the mechanical power that is required for an Earth-to-orbit first stage to achieve mission-average specific impulse, large area ratios are desired. Therefore, because the flow is overexpanded at sea-level launch conditions, the structural design of the nozzle wall is driven by the maximum allowable buckling loads that form during startup. That is, the pressure ratio during startup is below the design pressure ratio of the nozzle, which causes the expanding gas to separate from the nozzle wall. High-area-ratio nozzles with wall-separated flows are incubators for shock wave–boundary layer interactions (SWBLI), thermal and material stresses and a turbulent recirculation zone. These complicated flow and shock patterns produce off-axis side loads, which couple with the nozzle to produce fluid–structure interactions with sufficient strength to cause structural failure of the nozzle (Nave & Coffey 1973). Many independent investigations (Chen, Chakravarthy & Hung 1994; Nasuti & Onofri 1998; Hagemann, Frey & Koschel 2002; Ostlund 2002) have identified the existence of two kinds of separated nozzle flow regimes. There are free shock separation (FSS) and restricted shock separation (RSS); a review of the literature describing these kinds of flow states is provided by Hadjadj & Onofri (2009). Thus, an understanding of the loads produced by these different flow separation regimes is paramount to the safety and reliability of current and future rocket launch systems.

The type of shock pattern (FSS or RSS) that forms inside the nozzle is dependent on the shape of the nozzle wall and the nozzle pressure ratio (NPR; ratio of plenum pressure p_0 to ambient pressure p_a). Truncated ideal contour (TIC) nozzles display only the FSS type, which is shown in figure 1(*a*). For FSS flow, an adverse pressure gradient forms along the nozzle wall that causes the flow to separate, resulting in the consequent formation of compression waves that coalesce to form a conical separation shock. In conical nozzles, shock-induced separation occurs when the ratio of the wall pressure and the ambient pressure is between 0.2 and 0.4, depending on the design Mach number (Stark 2013). In figure 1(*a*), reflection of the separation shock on the nozzle axis of symmetry is shown to produce a Mach disk and a second oblique leg (reflected shock). These three shocks meet at the so-called triple point. This type of interaction is named *free* since the separated shear layer never reattaches to the nozzle wall. In thrust optimized contour (TOC) and thrust optimized parabolic (TOP) nozzles, as the NPR increases, the flow transitions from FSS flow to RSS flow; the pressure ratio that governs the FSS to RSS transition is unique to each nozzle contour. Figure 1(*b*) identifies the general features of RSS flow, which is characterized by a cap-shock pattern (Nave & Coffey 1973) and the reattachment of the separated shear layer to the wall with a large recirculation bubble (not shown in the figure) on the nozzle centreline (Nasuti & Onofri 1998).

The earliest reports on nozzle side loads proposed that oscillations of the internal shock system inside the nozzle were the main drivers for off-axis side loads. For TOP and TOC nozzles, side loads peak when the flow undergoes FSS to RSS transition (Frey & Hagemann 2000; Ostlund 2002). Earlier efforts turned towards developing analytical and empirical tools capable of predicting the occurrence of side loads based on statistical models of the shock motion. For example, Schmucker (1984) developed a model based on the idea of a tilted separation line, while Dumnov (1996) considered oscillations of the separation line excited by random pressure pulsations in the separated flow region. These methods rely on many simplifications and are primarily tailored for use as design tools. As both numerical and experimental disciplines have

Downloaded from https://www.cambridge.org/core. IP address: 151.24.234.247, on 27 May 2020 at 05:31:14, subject to the Cambridge Core terms of use, available at https://www.cambridge.org/core/terms. https://doi.org/10.1017/jfm.2020.280

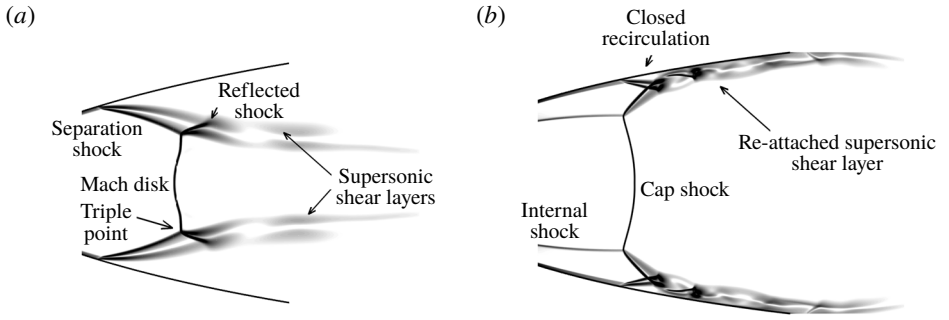

FIGURE 1. Schematic of the two common flow regimes that form inside the diverging section of high-area-ratio supersonic nozzles. (*a*) Free shock separation flow found in TIC, TOC and TOP nozzles. (*b*) Restricted shock separation flow found in TOC and TOP nozzles.

made numerous advances in the past two decades, the focus is being directed towards developing a more physical understanding of the underlying mechanisms responsible for these lateral forces.

The present work focuses on the FSS pattern, which is common to all supersonic nozzles and is characterized by intense side-load activity (Ruf, McDaniels & Brown 2010). Numerous efforts have been made to characterize the unsteady wall pressure during FSS flow. In particular, Baars *et al.* (2012) and Baars & Tinney (2013) showed that the unsteady wall pressure of a cold-gas, subscale parabolic nozzle during FSS flow is characterized by broad low- and high-frequency peaks associated with SWBLI and turbulent shear layer development, respectively. Those authors were able to isolate the effect of the asymmetric azimuthal mode, which is the mode responsible for generating side loads. More recently, Jaunet *et al.* (2017) observed the evolution of the FSS pattern and the associated Fourier azimuthal modes by varying NPR in a subscale TIC nozzle. They showed how low-frequency fluctuations in the pressure field are primarily asymmetric and are confined to the interior regions of the nozzle. However, the developing turbulent shear layer was shown to comprise high-frequency signatures in the pressure and velocity fields and were observed both inside and outside of the nozzle. Jaunet *et al.* (2017) also found highly organized pressure structures at an intermediate-frequency range, mainly associated with the asymmetric pressure mode, and argued that the structures were attributed to a screech-like mechanism (Raman 1999; Edgington-Mitchell 2019) as opposed to transonic resonance (Wong 2005).

Experimental efforts seem to suggest that the various frequency and azimuthal modes inside the nozzle are general features of the FSS pattern. However, experiments on axisymmetric nozzles suffer from the lack of flow measurements inside the nozzle itself, due to the challenging flow conditions and limited optical access. Therefore, numerical simulations can be leveraged as a complementary tool to gain insight into the internal flow physics of separated rocket nozzle flows, and to provide a pathway for addressing important outstanding questions. Of particular interest is a desire to better understand the kinds of frequencies and flow modes that characterize the vortices in the initial part of the supersonic shear layer. Furthermore, if a screech-like mechanism is present due to the interaction of the turbulent shear layer and the shock cell inside the jet, then it is of interest to understand the role of the Mack disk and subsonic flow region in the feedback loop.

Downloaded from https://www.cambridge.org/core. IP address: 151.24.234.247, on 27 May 2020 at 05:31:14, subject to the Cambridge Core terms of use, available at https://www.cambridge.org/core/terms. https://doi.org/10.1017/jfm.2020.280

Unsteady Reynolds-averaged Navier–Stokes (RANS) equations have been used in the past to evaluate the side loads produced by subscale models, and with rather accurate results being obtained (Deck & Guillen 2002; Deck & Nguyen 2004). However, modelling the global effect of the turbulent scales, as done in the unsteady RANS approach, could mask some of the important features relevant to the formation of unsteady aerodynamic loads. On the other hand, a direct numerical simulation of this kind of flow, characterized by Reynolds numbers of the order of 10^7, is impractical given the extremely high computational expense. The same is true for a wall-resolved large-eddy simulation (LES). Therefore, a practical alternative to unsteady RANS equations, direct numerical simulation and LES is the use of the detached eddy simulation (DES) method described by Spalart *et al.* (1997). The DES method comprises a hybrid of RANS and LES methods and allows high-Reynolds-number flows comprising massive flow separation to be modelled. In fact, in the DES approach, attached boundary layers are treated in RANS mode (thus lowering the computational requirements), while the most energetic turbulent scales of the separated shear layers and turbulent recirculating zones are treated directly in LES mode. As shown by a series of recent studies (Martelli *et al.* 2017, 2019; Memmolo, Bernardini & Pirozzoli 2018), the DES method has proven to be a powerful tool for investigating the flow physics of SWBLI involving massive flow separation where the dynamics is mainly characterized by the dominance of downstream effects (Clemens & Narayanaswamy 2014; Estruch-Samper & Chandola 2018). However, very few DES simulations of separated rocket nozzle flows are discussed in the open literature. Deck (2009) and Shams *et al.* (2013) presented a delayed DES (DDES) of the end-effect regime in an axisymmetric nozzle flow characterized by RSS. While the simulation reproduced the main flow properties rather well, the most energetic frequency, as predicted by the simulation, was higher than that observed in the experiment. As far as FSS is concerned, to the best of the authors' knowledge, the only DES available has been reported by Larusson, Andersson & Ostlund (2016), who exclusively focused on the prediction of the side-load magnitude.

In this study, we present the results of a DES of a TIC nozzle with flow separation. The geometry has been tested at the University of Texas at Austin, where measurements of the unsteady wall-pressure signatures were recorded. The analysis focuses first on the behaviour of these wall-pressure signatures and on elucidating the underlying mechanisms responsible for generating aerodynamic loads. Numerical results are then used to investigate and characterize parts of the flow not easily accessible using conventional experiment instruments. These are the Mach disk region and the initial part of the annular supersonic shear layer.

The article is organized as follows. First, a description of the experimental apparatus and instrumentation is provided in § 2 followed by an overview of the DDES approach, the numerical solver and the computational set-up in § 3. The first set of results from the DDES model are then discussed in § 4 with an emphasis on the general features of the flow that forms inside a TIC nozzle. In § 5, the main features of the wall-pressure signatures are analysed by way of space–time correlations and spectral analysis. Section 6 focuses on a discussion of the dynamics of the annular shear layer and Mach disk, which play a key role in the existence of an aeroacoustic feedback loop, which we propose and discuss in § 7. A summary of the effort and conclusions are finally given in § 8.

Downloaded from https://www.cambridge.org/core. IP address: 151.24.234.247, on 27 May 2020 at 05:31:14, subject to the Cambridge Core terms of use, available at https://www.cambridge.org/core/terms. https://doi.org/10.1017/jfm.2020.280

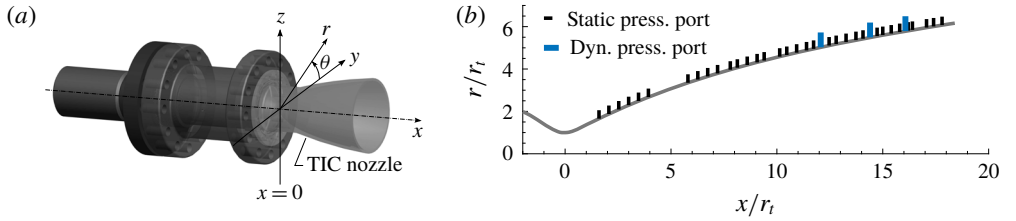

FIGURE 2. (*a*) Schematic of the nozzle with coordinate system. (*b*) The TIC nozzle contour identifying the axial locations of the static and dynamic pressure ports.

2. Main features of the experimental campaign

2.1. *Facility and nozzle test article*

The reduced-scale nozzle studied here has a TIC and was designed by the Nozzle Test Facility team at NASA Marshall Space Flight Center (Ruf, McDaniels & Brown 2009). An illustration of the nozzle contour is shown in figure 2(*a*) and comprises a throat radius of $r_t = 19.0$ mm, an exit radius of $r_e = 117.43$ mm and a throat-to-exit length of $L = 350.52$ mm. The nozzle's exit-to-throat area ratio of $A_e/A^* = 38$ results in a design exit Mach number of $M_d = 5.58$ at a NPR of 970. The length of the diverging nozzle contour is 79% of a 15° conical nozzle with the same area ratio and is a standard truncation length for TIC nozzles (Rao 1958).

All measurements were acquired in a fully anechoic chamber at the University of Texas at Austin. The chamber walls are treated with sound-absorbing material with a normal incidence sound absorption coefficient of 99 % above 100 Hz in order to minimize acoustic reflections from exciting the shear layer and internal flow. Interior dimensions (from wedge tip to wedge tip) are 5.8 m (length) $\times$ 4.6 m (width) $\times$ 3.7 m (height) with the nozzle centreline coinciding with the centreline of the chamber. Behind the nozzle is a 1.22 m $\times$ 1.22 m opening that supplies ambient air to the chamber that then exhausts through a 1.83 m $\times$ 1.83 m acoustically treated duct. Additional details of the facility, test article and data acquisition system are provided by Baars & Tinney (2013), Baars *et al.* (2014) and Donald *et al.* (2014).

The nozzle test rig functions as a blow-down type that is supplied with unheated air from a tank with a storage capacity of 4.25 m^3 of water volume at a pressure of 140 bar. The NPRs are monitored by a National Instruments CompactRIO system, which also controls a pneumatically actuated valve that regulates the plenum pressure during testing. Images of the TIC nozzle and test environment are shown in figure 3.

2.2. *Operating conditions and instrumentation*

For the current study, the TIC nozzle was operated at a constant NPR of nominally 30.7 for approximately 3 s. Both static and dynamic wall-pressure measurements were acquired during this run and will serve as the validation data for the DDES flow of the same nozzle contour and test conditions. Static wall pressures were measured using two Scanivalve DSA3218 gas pressure scanners, with a total of 34 static pressure ports sampled simultaneously at 500 Hz. These ports were oriented along the axial direction of the nozzle contour, between $x/r_t = 1.60$ and 17.80, as shown in figure 2(*b*), and provide a reliable means by which to infer the location of the separation shock.

For the fluctuating wall pressure, a total of six time traces are acquired using Kulite XT-140 dynamic pressure transducers sampled at $f_s = 100$ kHz. These sensors have

Downloaded from https://www.cambridge.org/core. IP address: 151.24.234.247, on 27 May 2020 at 05:31:14, subject to the Cambridge Core terms of use, available at https://www.cambridge.org/core/terms. https://doi.org/10.1017/jfm.2020.280

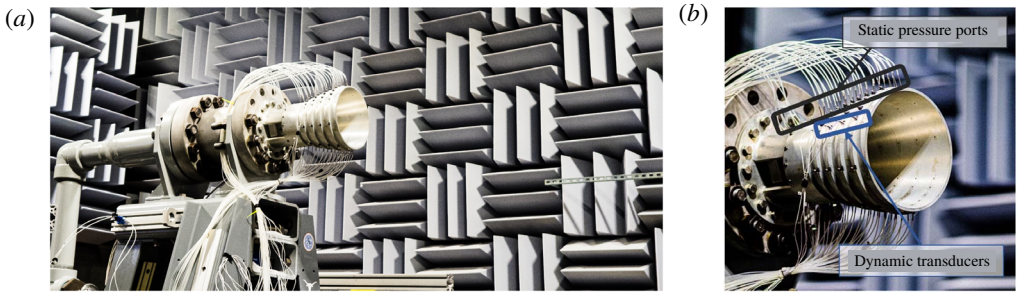

FIGURE 3. (*a*) Photo of the anechoic test environment at the University of Texas at Austin where the experiments were performed. (*b*) Photo of a nozzle installed on the test rig highlighting the tubing and wiring associated with the static and dynamic pressure ports.

a dynamic range of 100 psia (±0.1 % full-scale output), and were installed so that their protective B-type screens, with a 2.62 mm outside diameter, were flush with the interior surface. The screens limit the effective frequency response up to ~ 10 kHz (personal communication with the manufacturer). All channels were sampled simultaneously using appropriate signal conditioning from a National Instruments PXI-based system and were processed accordingly, so that resolved spectra up to 10 kHz were inferred (in combination with the associated root-mean-square wall-pressure amplitudes). Transducers were installed at three axial stations in the nozzle: $x/r_t = 12.07$, 14.40 and 16.73, with three transducers per axial location at two opposing azimuth angles. Figure 2 displays a schematic of the nozzle and the locations of the pressure ports.

3. Computational strategy

3.1. *Physical model*

The main body of this effort comprises a computational model of the flow produced by the same TIC nozzle contour as described in § 2. This model is constructed by solving the Reynolds averaged/filtered version of the three-dimensional Navier–Stokes equations for a compressible, viscous, heat-conducting gas:

$$\left.\begin{aligned} \frac{\partial \rho}{\partial t} + \frac{\partial (\rho\, u_j)}{\partial x_j} &= 0, \\ \frac{\partial (\rho\, u_i)}{\partial t} + \frac{\partial (\rho\, u_i u_j)}{\partial x_j} + \frac{\partial p}{\partial x_i} - \frac{\partial \tau_{ij}}{\partial x_j} &= 0, \\ \frac{\partial (\rho\, E)}{\partial t} + \frac{\partial (\rho\, E u_j + p u_j)}{\partial x_j} - \frac{\partial (\tau_{ij} u_i - q_j)}{\partial x_j} &= 0, \end{aligned}\right\} \tag{3.1}$$

where ρ is the density, u_i is the velocity component in the ith coordinate direction ($i = 1, 2, 3$), E is the total energy per unit mass and p is the thermodynamic pressure. According to the DES formulation, the variables in (3.1) can be interpreted as time-averaged or space-filtered quantities according to the branch (RANS or LES) assumed by the turbulence model. The total stress tensor τ_{ij} is the sum of the viscous and the Reynolds stress/subgrid-scale tensor:

$$\tau_{ij} = 2\,\rho\,(\nu + \nu_t)\, S^*_{ij} \quad S^*_{ij} = S_{ij} - \tfrac{1}{3}\, S_{kk}\, \delta_{ij}, \tag{3.2a,b}$$

Downloaded from https://www.cambridge.org/core. IP address: 151.24.234.247, on 27 May 2020 at 05:31:14, subject to the Cambridge Core terms of use, available at https://www.cambridge.org/core/terms. https://doi.org/10.1017/jfm.2020.280

where the Boussinesq hypothesis is applied through the introduction of the eddy viscosity ν_t, S_{ij} is the strain-rate tensor and ν is a kinematic viscosity that depends on temperature T through Sutherland's law. Similarly, the total heat flux q_j is the sum of molecular and turbulent contributions:

$$q_j = -\rho\, c_p \left(\frac{\nu}{Pr} + \frac{\nu_t}{Pr_t}\right) \frac{\partial T}{\partial x_j}, \tag{3.3}$$

where Pr and Pr_t are the molecular and turbulent Prandtl numbers, assumed to be 0.72 and 0.9, respectively.

3.2. *Turbulence modelling*

Because of the high Reynolds number of the flow produced by this TIC nozzle, the numerical methodology adopted here is the DDES (Spalart *et al.* 2006) belonging to the family of hybrid RANS/LES methods. Our implementation is based on the Spalart–Allmaras turbulence model, which solves a transport equation for a pseudo-eddy viscosity $\tilde{\nu}$:

$$\frac{\partial(\rho\tilde{\nu})}{\partial t} + \frac{\partial(\rho\,\tilde{\nu}\,u_j)}{\partial x_j} = c_{b1}\tilde{S}\rho\tilde{\nu} + \frac{1}{\sigma}\left[\frac{\partial}{\partial x_j}\left[(\rho\nu + \rho\tilde{\nu})\frac{\partial\tilde{\nu}}{\partial x_j}\right] + c_{b2}\,\rho\left(\frac{\partial\tilde{\nu}}{\partial x_j}\right)^2\right] - c_{w1}f_w\rho\left(\frac{\tilde{\nu}}{\tilde{d}}\right)^2, \tag{3.4}$$

where $\tilde{d}$ is the model length scale, f_w is a near-wall damping function, $\tilde{S}$ is a modified vorticity magnitude and σ, c_{b1}, c_{b2} and c_{w1} are model constants. The eddy viscosity in (3.2) is related to $\tilde{\nu}$ through $\nu_t = \tilde{\nu} f_{v1}$, where f_{v1} is a correction function designed to guarantee the correct boundary-layer behaviour in the near-wall region. In DDES, the destruction term in (3.4) is tailored in such a way that the model reduces to pure RANS for attached boundary layers and to a LES subgrid-scale model for flow regions detached from walls. This is accomplished by defining the following length scale $\tilde{d}$ so that

$$\tilde{d} = d_w - f_d \max\,(0,\, d_w - C_{DES}\,\Delta)\,, \tag{3.5}$$

where d_w is the distance from the nearest wall, Δ is the subgrid length scale that controls the wavelengths resolved in LES mode and C_{DES} is a calibration constant equal to 0.20. The function f_d, designed to be 0 in boundary layers and 1 in LES regions, is defined as

$$f_d = 1 - \tanh\left[(16 r_d)^3\right], \quad r_d = \frac{\tilde{\nu}}{k^2\, d_w^2\, \sqrt{U_{i,j}U_{i,j}}}, \tag{3.6a,b}$$

where $U_{i,j}$ is the velocity gradient tensor and k the von Kármán constant. The introduction of f_d distinguishes DDES from the original DES approach (Spalart *et al.* 1997) (denoted as DES97). It guarantees that boundary layers are treated in RANS mode even in the presence of particularly fine grids, when spacings in the wall-parallel directions are smaller than the boundary-layer thickness. This precaution is needed to prevent the phenomenon of modelled stress depletion, consisting of the excessive reduction of the eddy viscosity in the region of switch (grey area) between RANS and LES, which in turn can lead to grid-induced separation.

The subgrid length scale in this work depends on the flow itself through f_d such that

$$\Delta = \frac{1}{2}\left[\left(1 + \frac{f_d - f_{d0}}{|f_d - f_{d0}|}\right)\Delta_{max} + \left(1 - \frac{f_d - f_{d0}}{|f_d - f_{d0}|}\right)\Delta_{vol}\right], \tag{3.7}$$

Downloaded from https://www.cambridge.org/core. IP address: 151.24.234.247, on 27 May 2020 at 05:31:14, subject to the Cambridge Core terms of use, available at https://www.cambridge.org/core/terms. https://doi.org/10.1017/jfm.2020.280

where $f_{d0} = 0.8$, $\Delta_{max} = \max(\Delta x, \Delta y, \Delta z)$ and $\Delta_{vol} = (\Delta x \cdot \Delta y \cdot \Delta z)^{1/3}$. This definition is taken from Deck (2012) and is different from the original DDES formulation. The idea is to employ the f_d function as a switch between Δ_{max} (needed to shield the boundary layer) and Δ_{vol} (needed to ensure a rapid destruction of modelled viscosity). Suppressing modelled viscosity unlocks the Kelvin–Helmholtz instability and accelerates the switch to resolved turbulence in the separated shear layer. The problem of modelled stress depletion, the need of avoiding the delay in the onset of shear-layer instabilities and, more generally, the management of the hybridization strategy of RANS and LES are well-known challenges. These kinds of strategies are the subject of modelling efforts today (Haering, Oliver & Moser 2019).

3.3. *Flow solver description*

Simulations were carried out by means of an in-house compressible flow solver that solves the compressible Navier–Stokes equations on structured grids. For flow regions away from shocks, the spatial discretization consists of a centred, second-order, finite-volume scheme (Pirozzoli 2011). The approach is based on an energy-consistent formulation that makes the numerical method extremely robust without the addition of numerical dissipation (Pirozzoli 2011). This feature is particularly useful in the flow regions treated in LES mode, where in addition to the molecular viscosity, the only relevant viscosity should be the one provided by the turbulence model. Near discontinuities, identified by the Ducros shock sensor (Ducros *et al.* 1999), the scheme switches to third-order Weno reconstructions for cell-faced flow variables. Gradients normal to the cell faces, which are needed for viscous fluxes, are evaluated using second-order central-difference approximations that obtain compact stencils and avoid numerical odd–even decoupling phenomena. A low-storage, third-order Runge–Kutta algorithm (Bernardini & Pirozzoli 2009) is used for time advancement of the semi-discretized ordinary differential equation system. The code is written in Fortran 90 and uses domain decomposition while fully exploiting the message-passing interface paradigm for the parallelism. The accuracy and reliability of the DDES flow solver were addressed in recent SWBLI studies (Martelli *et al.* 2017, 2019; Memmolo *et al.* 2018).

3.4. *Test case description and computational set-up*

Simulation parameters were selected to reproduce the experimental conditions described in § 2.2 comprising a nozzle pressure ratio of 30.35, based on total and ambient pressures of $p_0 = 3.035$ MPa and $p_a = 0.1$ MPa, respectively. The total T_0 and ambient T_a temperatures were both valued at 300 K while the nozzle Reynolds number, evaluated with the throat radius, density ρ_0, speed of sound a_0 and molecular viscosity taken at the stagnation chamber condition $\mu_0 = \mu(T_0)$, is

$$Re = \frac{\rho_0 a_0 r_t}{\mu_0} = \frac{\sqrt{\gamma}}{\mu_0} \frac{p_0 r_t}{\sqrt{R_{air} T_0}} = 1.7 \times 10^7.$$

The three-dimensional computational domain was designed to include both the nozzle and an extended portion of the external ambient (for flow entrainment), as shown in figure 4. Starting from the nozzle throat, the outflow boundary is shown to extend 150 throat radii in the longitudinal direction and $76 r_t$ in the radial direction, relative to the nozzle axis. As for boundary conditions, total pressure, total temperature and flow direction are imposed at the nozzle inflow. A downstream pressure equal to p_a

Downloaded from https://www.cambridge.org/core. IP address: 151.24.234.247, on 27 May 2020 at 05:31:14, subject to the Cambridge Core terms of use, available at https://www.cambridge.org/core/terms. https://doi.org/10.1017/jfm.2020.280

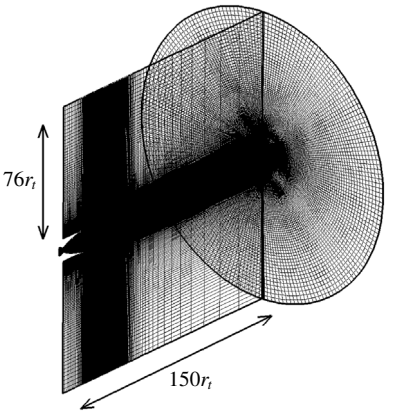

FIGURE 4. Schematic of the computational mesh used in the DDES model of the TIC nozzle flow.

is prescribed on the outside boundaries, except for the outflow boundary to the right of the computational domain, where non-reflecting boundary conditions are imposed. Nozzle walls are treated by prescribing the no-slip adiabatic condition.

Mesh resolution was selected following a preliminary sensitivity study comprising steady-state axisymmetric RANS computations, for which convergence of the separation location was obtained. The number of cells in the azimuthal direction ($N_z = 192$) was then selected to guarantee approximately isotropic, cubic cells in the LES zone, leading to a final three-dimensional grid with approximately 85 million cells (see figure 4). The converged RANS solution was also used to initialize the three-dimensional DDES computation. It is worth pointing out that, due to the specific form of the DDES blending functions to switch between RANS and LES branches, the flow region including the separation point in the present three-dimensional computation is treated in RANS mode. To promote the development of turbulent structures and the switch from modelled to resolved turbulence, the streamwise velocity was seeded with random perturbations at the onset of the simulation with a maximum magnitude of 3 % of the inflow velocity.

The computation ran with a time step $\Delta t = 6.2 \times 10^{-8}$ s for a total duration of $T = 0.083$ s, which guarantees coverage of frequencies down to $f_{min} \approx 12$ Hz. A total of 500 fully three-dimensional fields were then recorded at time intervals of 1.66×10^{-4} s for post-processing purposes. On the contrary, wall pressures and pressure fields along discrete azimuthal planes were recorded at shorter time intervals of 3.1×10^{-6} s in order to resolve a broader range of frequencies needed in subsequent analysis. The cost of the simulation was approximately 3.17 Mio CPU hours and used 2304 processors on the Tier-0 system Marconi (Cineca supercomputing facility).

4. Flowfield characteristics

The salient features of the FSS pattern are illustrated in figure 5 using Mach number contours obtained by averaging the simulated flow in both azimuth and time. Because the flow is in an overexpanded state, a shock system appears inside the nozzle, which adapts the exhaust pressure to the ambient pressure. Consequently, the strong adverse pressure gradient induced by the shock causes the flow to

Downloaded from https://www.cambridge.org/core. IP address: 151.24.234.247, on 27 May 2020 at 05:31:14, subject to the Cambridge Core terms of use, available at https://www.cambridge.org/core/terms.
https://doi.org/10.1017/jfm.2020.280

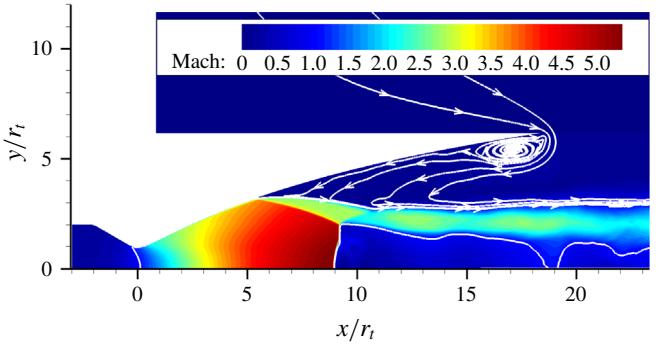

FIGURE 5. Contours of the averaged Mach number field from DDES. The white solid line denotes the sonic level. Streamtraces are also reported to highlight the open recirculation region.

separate from the wall thereby resulting in the formation of a detached shear layer. Downstream of this shock-induced separation, the wall region is dominated by a subsonic recirculating flow that continuously entrains ambient air. This shock system comprises a conical shock, which is reflected as a Mach disk on the nozzle axis. The reflection is completed by a second conical shock, which deflects the inclined supersonic annular jet in a direction nearly parallel to the nozzle axis. Immediately following the Mach disk, the flow is initially subsonic, before it eventually expands and, through a fluid-dynamic throat, accelerates up to supersonic velocities resulting in the occurrence of a new shock that adapts the jet flow to ambient pressure. The flow pattern resembles that of a classical overexpanded jet but, contrary to lower-Mach-number nozzles (e.g. aeronautical propulsion systems), the jet starts well inside the nozzle as opposed to a shock system emanating from the nozzle lip under full-flowing conditions. The wall boundary-layer thickness (based on 99 % of the external velocity u_e) just ahead of the separation point is $\delta_{99} = 0.098r_t$, while the edge Mach number is $M_e = 3.38$ ($u_e = 623.83$ m s^{-1}).

The unsteady nature of this flow is demonstrated in figure 6 by showing contours of the instantaneous density-gradient magnitude along a slice through the centre of the nozzle, and in figure 7 using isosurfaces of the Q criterion (Hunt, Wray & Moin 1988). The latter is a well-known qualitative method used to identify tube-like vortical structures and in this analysis it has been modified to account for the effect of compressibility (Pirozzoli, Bernardini & Grasso 2008). Let $A = \boldsymbol{\nabla u}$ be the gradient velocity tensor and $A^* = (A - \frac{1}{3}\boldsymbol{\nabla} \cdot \boldsymbol{u}\boldsymbol{I})$ its traceless part. Turbulent structures are extracted by visualizing regions with a positive iso-value of the second invariant of A^*, defined as $Q^* = -\frac{1}{2}A^*_{ij}A^*_{ji}$, since in these regions rotation exceeds the strain. Various patterns are visible in figures 6 and 7, including the generation of large turbulence structures in the annular supersonic shear layer, the sudden break-up of the jet core downstream and the radiation of weak Mach waves at shallow angles to the jet axis. These Mach waves are observed in the shadowgraphy images of Canchero *et al.* (2016) and corroborate the findings shown here. The isosurfaces also demonstrate how the initial part of the shear layer is not dominated by azimuthally coherent rollers, which are typical of low-Reynolds-number incompressible mixing layers. In the present case, oblique modes are shown to dominate the initial part of the shear layer, leading to small-scale three-dimensional structures. This change is due to the large local convective Mach number ($M_c \approx 1.03$) at the beginning of the

Downloaded from https://www.cambridge.org/core. IP address: 151.24.234.247, on 27 May 2020 at 05:31:14, subject to the Cambridge Core terms of use, available at https://www.cambridge.org/core/terms. https://doi.org/10.1017/jfm.2020.280

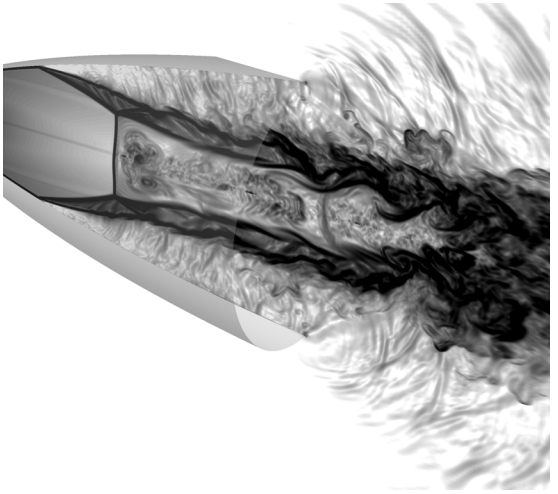

FIGURE 6. Visualization of the instantaneous density-gradient magnitude (numerical schlieren) along a slice through the centre of the nozzle.

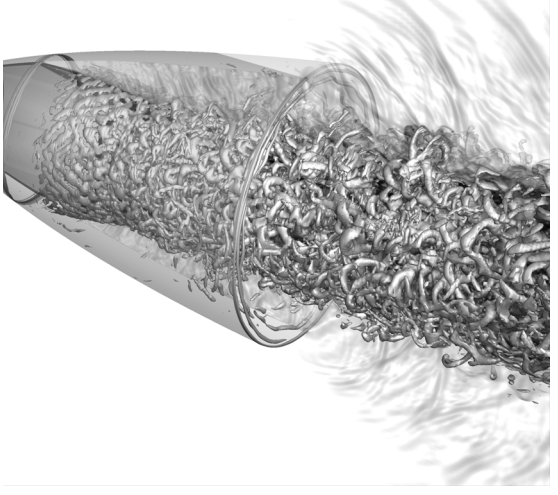

FIGURE 7. Visualization of turbulent structures using isosurfaces of the Q^* criterion.

shear layer, in agreement with the findings of Sandham & Reynolds (1991), who demonstrated that when $M_c > 1$, oblique modes dominate the instability process in planar compressible shear layers. Similar structures were observed by Simon *et al.* (2007) in the supersonic annular shear layer past an axisymmetric trailing edge, characterized by a convective Mach number greater than one.

5. Wall-pressure characteristics

5.1. *Mean and standard deviation distribution*

The mean wall-pressure distribution ($\overline{p}_w$), averaged in azimuth and time, is shown in figure 8(*a*) alongside static wall-pressure data from the experiment. Wall pressures are shown to decrease until the incipient separation point, after which the separation

Downloaded from https://www.cambridge.org/core. IP address: 151.24.234.247, on 27 May 2020 at 05:31:14, subject to the Cambridge Core terms of use, available at https://www.cambridge.org/core/terms.
https://doi.org/10.1017/jfm.2020.280

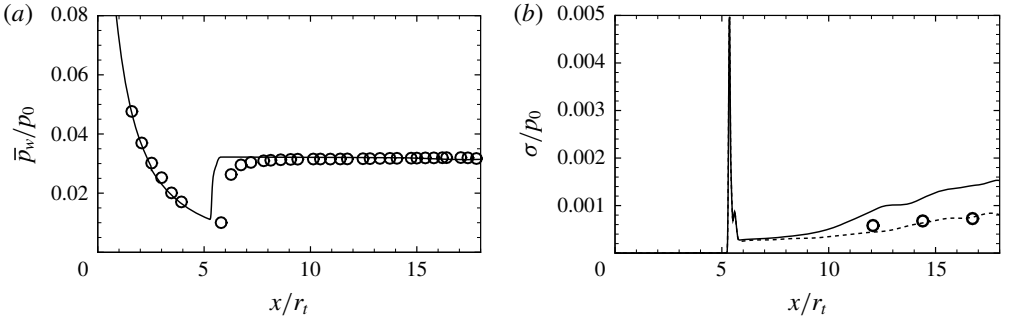

FIGURE 8. Distribution of (*a*) mean wall pressure and (*b*) standard deviation of the wall-pressure fluctuations. Solid line, DDES; open circles, reference experimental data. For the standard deviation of the DDES, a dashed line is representative of the pressure fluctuations below 10 kHz; experimental data are resolved up to that frequency.

shock causes an abrupt increase up to a plateau value close to ambient pressure. Data from the simulation illustrate the same findings as the experiment, except for the subtle discrepancy in the average separation shock location. This small discrepancy is attributed to two factors. The first is the unavoidable delay in the transition from RANS to LES mode (Shur *et al.* 2015) in the simulation, whereas the second is attributed to experimental uncertainties in the pressure-sensing system that measures NPR; these errors are estimated to be around 1 %.

As for the fluctuating wall pressure, the standard deviations (σ) from both the simulation and experiment are shown in figure 8(*b*). The solid line corresponds to the DDES data and reflects the axial behaviour of σ that is typical of a SWBLI footprint (Dolling & Or 1985; Baars, Ruf & Tinney 2015). That is, wall-pressure fluctuations are characterized by a dominant sharp peak at the separation shock location (due to shock foot oscillations that result in high and low pressures found downstream and upstream of the shock, respectively). Downstream of this oscillating shock region, pressure fluctuations relax, followed by gradual increases in fluctuation intensity with downstream distance along the nozzle wall; this is the consequence of increased intensity from Mach waves emanating from the developing separated turbulent shear layer. In order to validate the magnitude of the pressure fluctuations with the experimental data, a dashed line has been inserted in figure 8(*b*), whereby only the fluctuating energy up to 10 kHz is used to compute σ. That is, spectra are only integrated up to 10 kHz, following Parseval's theorem. This dashed line is in close agreement with the three experimental data points (only those pressure fluctuations below 10 kHz are considered accurate in the experiment). Since the standard deviation is an integral measure of the spectrum, it will be commented on further in § 5.2 where spectral signatures are considered.

5.2. *Frequency spectra*

Premultiplied wall-pressure power spectral densities, $G_{pp}(f) \cdot f/\sigma^2$, are shown in figure 9 as functions of both the longitudinal coordinate x and frequency f. Doing so provides a more complete picture of the spatial distribution of the energy along the nozzle wall and of the contribution of the different frequencies to the total energy of the signal. Power spectral densities are estimated using Welch's method,

Downloaded from https://www.cambridge.org/core. IP address: 151.24.234.247, on 27 May 2020 at 05:31:14, subject to the Cambridge Core terms of use, available at https://www.cambridge.org/core/terms.
https://doi.org/10.1017/jfm.2020.280

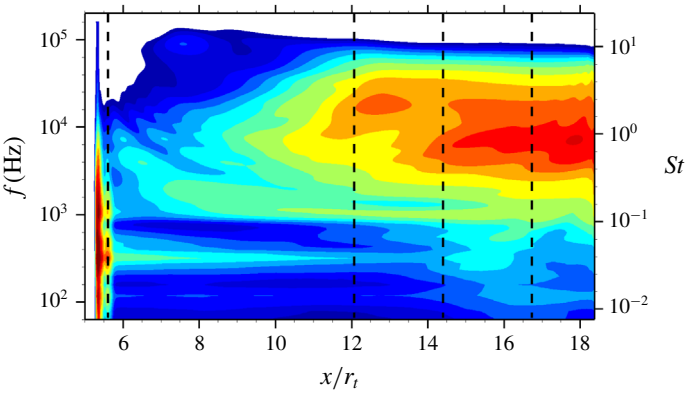

FIGURE 9. Contours of the premultiplied power spectral densities, $G_{pp}(f) \cdot f/\sigma^2$, of the wall-pressure signals as a function of the streamwise location and frequency. Sixteen contour levels are shown in exponential scale between 10^{-4} and 1.

i.e. subdividing the overall pressure record into 12 segments with 50 % overlap that are then individually Fourier-transformed. Frequency spectra are then obtained by averaging the periodograms of the various segments, thus minimizing the variance of the power spectral density estimator. For visualization purposes, a bandwidth moving filter, based on Konno–Ohmachi smoothing (Konno & Ohmachi 1998), has been applied, which results in a constant bandwidth on a logarithmic scale.

The spectral map in figure 9 reveals two regions with high fluctuating energy. The first region is located at the separation point ($x/r_t = 5.6$), where the signature of the shock motion is visible and is characterized by a broad peak in the low-frequency range and a narrow footprint in the spatial direction. The second region is located downstream in the high-frequency range ($f \approx 10$ kHz) and is associated with the developing separated shear layer, whose convected vortical structures radiate pressure disturbances that increase in intensity downstream. The overall spatial-spectral distribution of the fluctuating pressure along the expanding wall of this TIC nozzle is shown in figure 9 to be qualitatively similar to the canonical SWBLI measurements of Dupont, Haddad & Debiève (2006), despite the significant differences in the geometrical configuration and shock topology (open separation bubble) of the present flow case.

To assist with the experimental–numerical validation of this TIC nozzle flow, premultiplied spectra of the fluctuating wall-pressure footprint are shown in figure 10(*a–d*) for the four representative axial stations corresponding to the vertical lines in figure 9. Note that, for the purpose of comparison, the curves are normalized by the integral of the spectra over the range of frequencies that are being resolved by the experiment (10 kHz). The first position is located immediately downstream of the separation point ($x/r_t = 5.6$), whereas the other three correspond to positions where experimental data from the dynamic Kulite transducers are available ($x/r_t = 12.07$, $x/r_t = 14.40$ and $x/r_t = 16.73$). At $x/r_t = 5.6$ in figure 10(*a*), the spectrum corresponding to the shock motion shows the presence of a broad, high-amplitude bump between 100 Hz and 2 kHz, with a maximum at $f \approx 320$ kHz and a secondary peak at intermediate frequencies around $f \approx 1$ kHz. Baars *et al.* (2015) ascribed the low-frequency peak to an acoustic resonance (e.g. Wong 2005; Zaman *et al.* 2002).

Downloaded from https://www.cambridge.org/core. IP address: 151.24.234.247, on 27 May 2020 at 05:31:14, subject to the Cambridge Core terms of use, available at https://www.cambridge.org/core/terms. https://doi.org/10.1017/jfm.2020.280

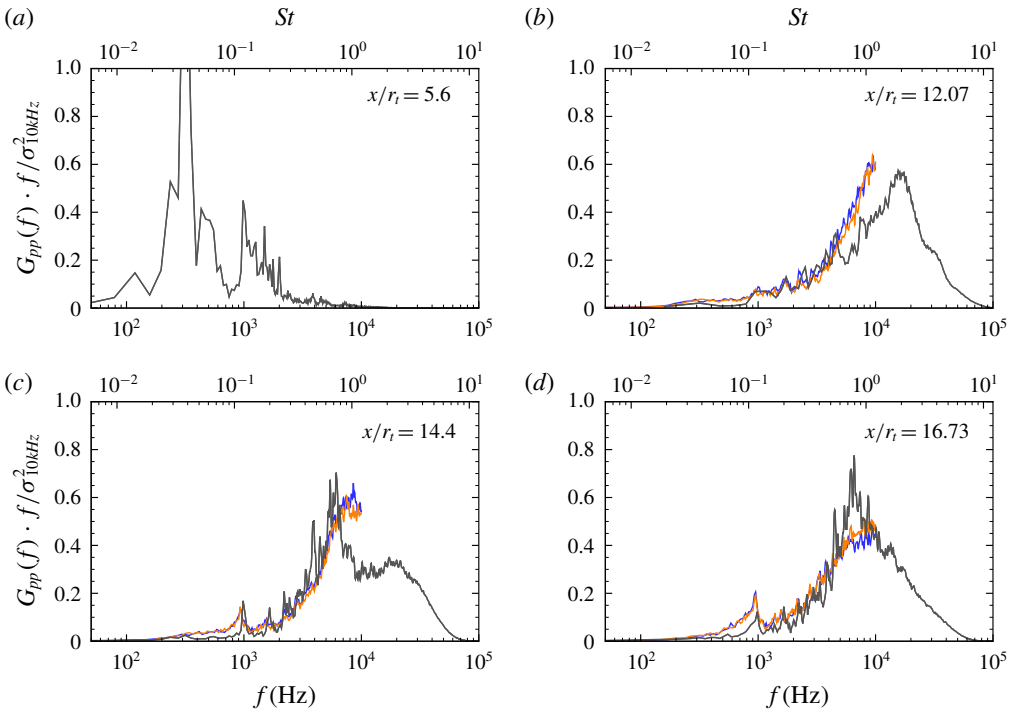

FIGURE 10. (*a–d*) Premultiplied power spectral densities of the wall-pressure signals at four different x locations. The solid grey line corresponds to the DDES, whereas the blue/orange lines correspond to the two experimental transducers at different azimuthal angles. Experimental data are only available for the locations of (*b–d*).

This resonance equates to a one-quarter acoustic standing wave whose fundamental frequency can be modelled using an open-ended pipe of length L as follows:

$$f_{ac} = \frac{a_\infty(1 - M_{NE}^2)}{4L} \approx 340 \text{ Hz}, \tag{5.1}$$

where $a_\infty = 345$ m s^{-1} is the ambient speed of sound and M_{NE} is the Mach number in the separated region at the nozzle exit. Here the pipe length is replaced by the distance between the incipient separation shock and the nozzle exit plane so that $L = 0.247$ m. The value of f_{ac} compares favourably with the 320 Hz spectral peak in figure 10(*a*). Moving downstream, a different picture emerges, where spectra are characterized by high frequencies ($f \approx 10$ kHz) attributed to signatures from the formation of turbulent structures in the developing shear layer. As expected, the peak frequency is shown to shift towards lower frequencies with increasing downstream position along the wall. A peak located at intermediate frequencies ($f \approx 1$ kHz) is still visible in the spectra downstream of the shock foot. These peaks are imprints of the 1 kHz frequency peak observed in figure 10(*a*) at $x/r_t = 5.6$.

The nature of this 1 kHz tone observed in both the numerical and experimental spectra is shown to agree reasonably well up to the maximum reliable frequency threshold of the measurements. Likewise, the main features of the power spectral densities in figure 10(*a–d*) are also found in previous experiments involving different

Downloaded from https://www.cambridge.org/core. IP address: 151.24.234.247, on 27 May 2020 at 05:31:14, subject to the Cambridge Core terms of use, available at https://www.cambridge.org/core/terms. https://doi.org/10.1017/jfm.2020.280

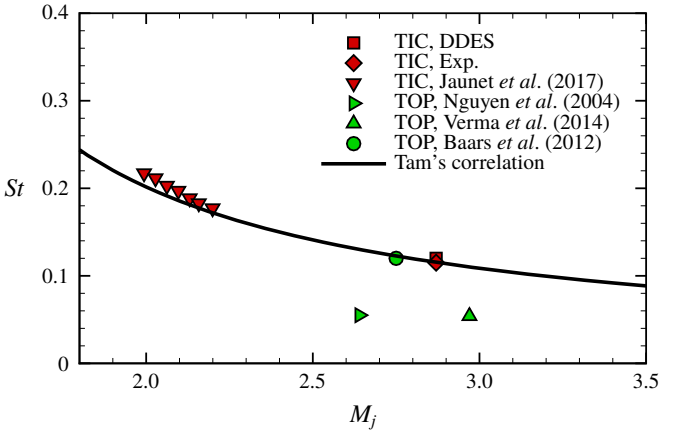

FIGURE 11. Strouhal number of the intermediate peak in the frequency spectrum at the shock position as a function of the fully adapted Mach number M_j for different geometries and NPRs.

TIC nozzle contours (Jaunet *et al.* 2017), or TOP nozzles operating at NPRs corresponding to FSS flow (Nguyen *et al.* 2003; Baars *et al.* 2012; Verma & Haidn 2014). To better characterize this 1 kHz intermediate peak, it is useful to introduce a Strouhal number, defined as (Tam, Seiner & Yu 1986; Canchero *et al.* 2016)

$$St = f\frac{D_j}{U_j}, \tag{5.2}$$

where U_j is the fully expanded jet velocity, given by

$$U_j = \sqrt{\gamma R T_0}\frac{M_j}{\sqrt{1+\dfrac{\gamma-1}{2}M_j^2}}, \tag{5.3}$$

where T_0 is the stagnation temperature, γ is the specific heat ratio, R is the air constant and M_j is the fully adapted Mach number which is a function of the NPR through the isentropic relation

$$M_j^2 = \frac{2}{\gamma-1}\left[(NPR)^{(\gamma-1)/\gamma}-1\right]. \tag{5.4}$$

The length scale D_j is computed as a function of M_j, the design Mach number M_d and the nozzle exit diameter D through the mass flux conservation:

$$\frac{D_j}{D} = \left(\frac{1+\dfrac{\gamma-1}{2}M_j^2}{1+\dfrac{\gamma-1}{2}M_d^2}\right)^{\frac{(\gamma+1)}{(4(\gamma-1))}}\left(\frac{M_d}{M_j}\right)^{1/2}. \tag{5.5}$$

The non-dimensional frequencies of the intermediate peak from the different experimental flow cases cited above are reported in figure 11 as a function of M_j.

Downloaded from https://www.cambridge.org/core. IP address: 151.24.234.247, on 27 May 2020 at 05:31:14, subject to the Cambridge Core terms of use, available at https://www.cambridge.org/core/terms.
https://doi.org/10.1017/jfm.2020.280

A decreasing trend of St with the fully adapted Mach number emerges, which was also identified by Jaunet *et al.* (2017). They proposed that this peak could be attributed to a screech-like mechanism (Raman 1999) resulting from an aeroacoustic feedback loop involving downstream-propagating disturbances in the shear layer interacting with the shock cells to form upstream-propagating acoustic waves that excite the shear layer. According to Tam *et al.* (1986) the screech frequency f_{sc} can be evaluated as

$$St_{sc} = f_{sc}\frac{D_j}{U_j} = 0.67(M_j^2 - 1)^{-1/2}\left[1 + 0.7M_j\left(1 + \frac{\gamma - 1}{2}M_j^2\right)^{-1/2}\left(\frac{T_a}{T_0}\right)^{-1/2}\right], \quad (5.6)$$

where T_a is the ambient temperature. The trend from the correlation in figure 11 shows that the characteristic screech frequency decreases with increasing M_j (or equivalently with increasing NPR), mainly due to the increase in shock cell spacing. Despite a certain level of dispersion, the proximity of the experimental data and of the DDES prediction to the theoretical correlation suggests that the intermediate peak could be attributed to a screech-like phenomenon associated with the shock cell structure present within the nozzle. Nevertheless, it must be pointed out that the shock cell spacing used in Tam's model, which is derived from a parallel flow assumption (Pack 1950), is $L/D_j = 2.81$. This model is usually adopted to study under- and overexpanded jets, without flow separation. Instead, the configuration investigated here manifests a large recirculation region inside the nozzle, with a Mach reflection characterized by the angle of the oblique shock, which is very different from $\pi/2$ (with respect to the nozzle longitudinal axis). As a consequence we have two characteristic distances $L_{s,1} = 2.38D_j$ and $L_{s,2} = 3.35D_j$, corresponding to the distances from the Mach disk and separation shock foot to the second normal shock, respectively. A feedback-loop model adapted to accommodate the unique flow and shock pattern produced by this TIC nozzle is proposed and discussed in § 7. There it will be shown that the larger length scales of the present configuration are partially compensated by characteristic velocities that differ from what was applied in Tam's model, thereby offering good agreement with the corollary of (5.6) for the present flow case.

5.3. *Space–time correlations and convection velocity*

Additional insights into the propagation of pressure disturbances, in terms of direction and velocity, can be gained by inspection of the space–time correlation coefficient, defined as

$$C_{pp}(x, \Delta x, \Delta\theta, \Delta\tau) = \frac{R_{pp}(x, \Delta x, \Delta\theta, \Delta\tau)}{\left[R_{pp}(x, 0, 0, 0)\right]^{1/2}\ \left[R_{pp}(x, \Delta x, 0, 0)\right]^{1/2}}, \quad (5.7)$$

where

$$R_{pp}(x, \Delta x, \Delta\theta, \Delta\tau) = \langle p_w'(x, \theta, t)\, p_w'(x + \Delta x, \theta + \Delta\theta, t + \Delta\tau)\rangle \quad (5.8)$$

is the space–time correlation function, Δx and $\Delta\theta$ are the spatial separations in the streamwise and azimuthal directions, $\Delta\tau$ is the time delay and $\langle\ \rangle$ denotes averaging with respect to the azimuthal direction (exploiting homogeneity) and time. Figure 12(*a*,*b*) reports contours of this space–time correlation coefficient $C_{pp}(x, \Delta x, 0, \Delta\tau)$ taken at two stations along the nozzle wall at $x/r_t = 8$ and

Downloaded from https://www.cambridge.org/core. IP address: 151.24.234.247, on 27 May 2020 at 05:31:14, subject to the Cambridge Core terms of use, available at https://www.cambridge.org/core/terms. https://doi.org/10.1017/jfm.2020.280

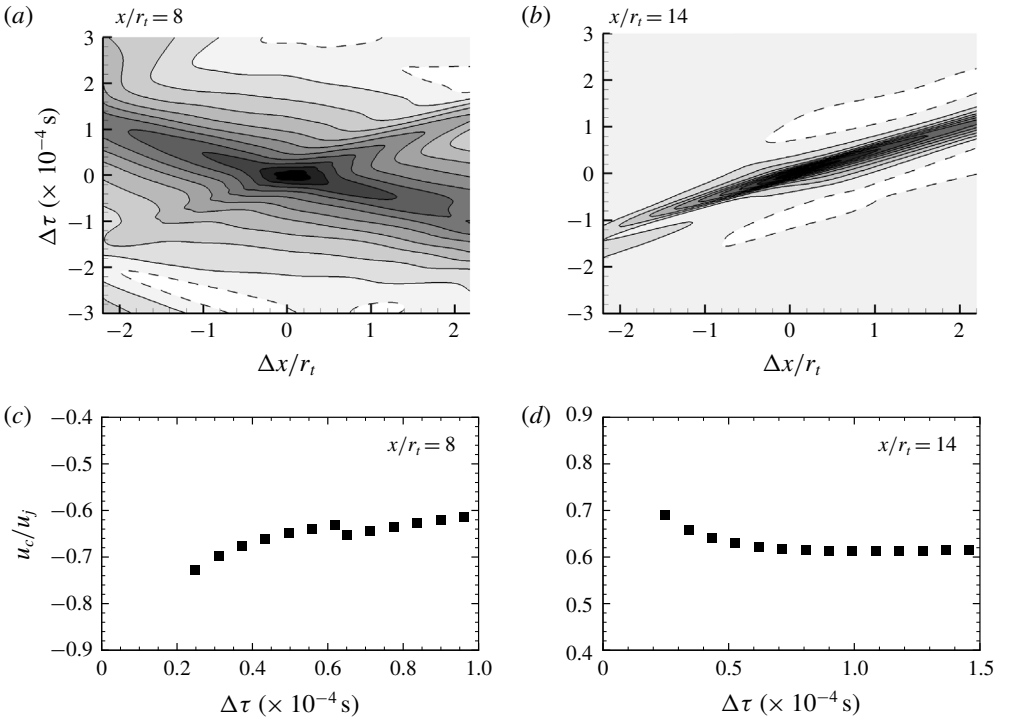

FIGURE 12. (*a*,*b*) Space–time contours of the pressure correlation coefficient $C_{pp}(\Delta x,\ 0,\ \Delta\tau)$ using 11 contour levels in the range $-0.1 < C_{pp} < 0.9$. (*c*,*d*) Local convection velocity of wall-pressure fluctuations as a function of the time separation $\Delta\tau$.

$x/r_t = 14$. At both positions, the shapes of the contours reflect the convective nature of the pressure field. Albeit, the pressure signal is mainly characterized by a coherent downstream propagation of pressure-carrying eddies at the downstream station ($x/r_t = 14$), while at the upstream location ($x/r_t = 8$) the presence of upstream-propagating disturbances is well visible.

From the maps of the space–time correlation coefficient it is possible to evaluate the convection velocities of the pressure-carrying eddies. Following Bernardini & Pirozzoli (2011), the convection speed corresponding to a given time delay $\Delta\tau$ is defined as the ratio $\Delta x/\Delta\tau$ taken at the spatial separation value Δx where a local maximum of C_{pp} is attained. The resulting convection speeds are displayed in figure 12(*c*,*d*), as a function of the time separation $\Delta\tau$. We see that the convection speeds range from $0.6u_j$ to $0.7u_j$, in agreement with the value quoted by Tam *et al.* (1986). There is also an absence of upstream-propagating disturbances in the space–time map of figure 12(*b*) which reinforces the notion that the unsteady pressure field at $x/r_t = 14$ is dominated by signatures from energetic, high-frequency, downstream-travelling vortices in the separated shear layer.

For a more rigorous inspection of the propagation speeds of these disturbances, a frequency-dependent convection velocity $u_c(f)$ is computed according to the formulation proposed by Renard & Deck (2015):

$$u_c(f) = \frac{-2\pi f\, G_{pp}(f)}{\mathrm{Im}\left(G_{pp'}(f)\right)}, \tag{5.9}$$

Downloaded from https://www.cambridge.org/core. IP address: 151.24.234.247, on 27 May 2020 at 05:31:14, subject to the Cambridge Core terms of use, available at https://www.cambridge.org/core/terms.
https://doi.org/10.1017/jfm.2020.280

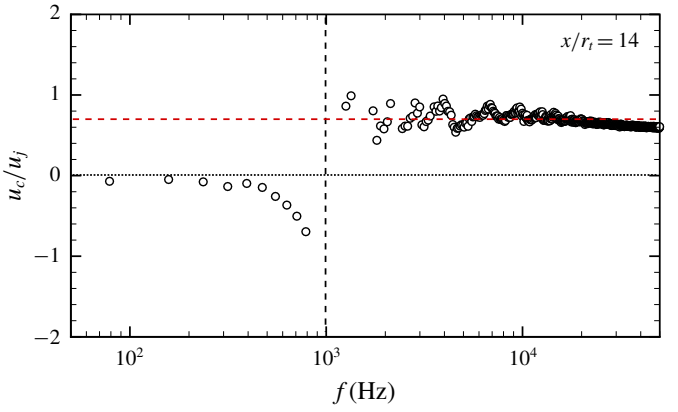

FIGURE 13. Frequency-dependent convection velocity at $x/r_t = 14$. The red horizontal dashed line denotes the value $0.7u_j$.

where $G_{pp'}$ is the cross-spectrum between the pressure signal and its streamwise derivative ($p' = \partial p/\partial x$). In the case of a simple monochromatic wave, equation (5.9) can be interpreted as the phase velocity, whereas in the general case its interpretation relies on the least-squares minimization of the convection equation residual, consistent with del Álamo & Jiménez (2009). This spectral approach is a generalization of previous methods based on the phase between signals taken at two streamwise points (Romano 1995). The upside to this approach is that it offers a direct assessment of scale dependence without having to band-pass filter the signals, thus preventing aliasing and/or phase alterations. Moreover, the method inherently includes the definition of a global convection velocity:

$$C_u = -\frac{\int_0^\infty (2\pi f)^2\ G_{pp}(f)\,\mathrm{d}f}{\int_0^\infty 2\pi f\,\mathrm{Im}(G_{pp'}(f))\,\mathrm{d}f}, \tag{5.10}$$

which can be shown to coincide with derived methods based on space–time correlations (Renard & Deck 2015). The distribution of u_c as a function of frequency f is reported in figure 13 for the probe at $x/r_t = 14$. The illustration clearly reveals how all frequencies leading up to the intermediate frequency of 1 kHz ($St = 0.12$) correspond to upstream-travelling waves. At this intermediate frequency, $u_c(f)$ diverges before switching to positive values. Such divergence could be explained by the formation of a standing wave arising from the interference of two travelling waves moving in the opposite direction that produce a zero phase value in the denominator of equation (5.9). This behaviour reinforces the postulation that the intermediate-frequency peak in the spectra is related to a screech-like process, which is classically associated with the formation of a standing wave generated by downstream-propagating hydrodynamic and upstream-propagating acoustic fluctuations (Tam 1995). Consistent with the results of the broadband analysis, the convection velocity associated with the high-frequency range in figure 13 is approximately equal to $0.7u_j$.

5.4. *Azimuthal decomposition of the pressure field*

In order to gain insights into the origins of the aerodynamic loads acting on the TIC nozzle wall, and to characterize the wavenumbers that make up the unsteady wall-pressure footprint, then it is natural to carry out a Fourier-azimuthal decomposition

Downloaded from https://www.cambridge.org/core. IP address: 151.24.234.247, on 27 May 2020 at 05:31:14, subject to the Cambridge Core terms of use, available at https://www.cambridge.org/core/terms.
https://doi.org/10.1017/jfm.2020.280

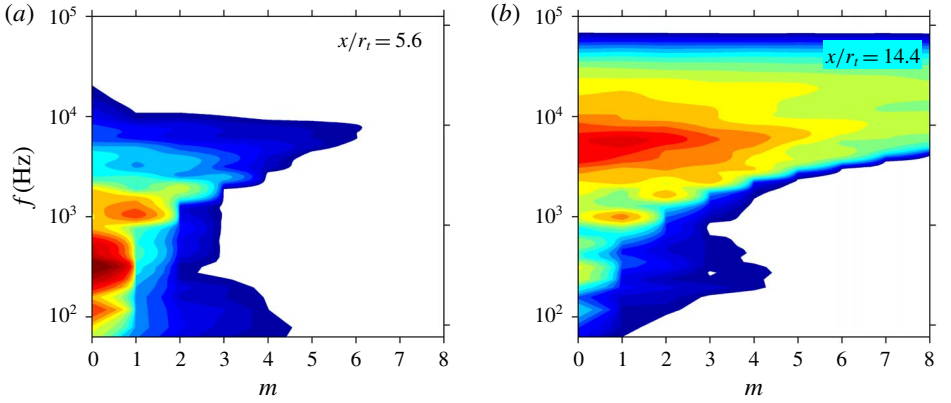

FIGURE 14. Contours of the premultiplied azimuthal wavenumber–frequency spectra $\phi_{pp}(f) \cdot f/\sigma^2$ at two different axial locations. Twenty contour levels are shown in exponential scale between 0.005 and 5.

of the fluctuating wall-pressure signatures. To that end, we consider the azimuthal wavenumber–frequency spectrum, defined as

$$\phi_{pp}(x, m, f) = \int_{-\infty}^{\infty} \int_{0}^{2\pi} R_{pp}(x, 0, \Delta\theta, \Delta\tau)\, \mathrm{e}^{-\mathrm{i}(m\Delta\theta + f\Delta\tau)} \mathrm{d}(\Delta\theta)\, \mathrm{d}(\Delta\tau), \tag{5.11}$$

where m is the Fourier-azimuthal wavenumber (or mode number). We remind ourselves that, according to symmetry, only the non-axisymmetric mode $m = 1$ will contribute to off-axis aerodynamic side loads.

The azimuthal wavenumber–frequency spectrum ϕ_{pp} is reported in figure 14 for two representative stations, corresponding to the location immediately downstream of the separation shock at $x/r_t = 5.6$ (figure 14*a*) and in the upstream-travelling entrained flow region at $x/r_t = 14.4$ (figure 14*b*). One can see that the preponderance of energy is confined to the first few Fourier-azimuthal modes, and is complementary to the experimental analysis of Baars & Tinney (2013). To better quantify the spectral make-up of the dominant azimuthal modes along the nozzle wall, slices through the wavenumber–frequency maps for the first two discrete azimuthal modes ($m = 0$ and $m = 1$) are reported in figure 15. This figure reveals how the shock motion at $x/r_t = 5.6$ in figure 15(*a*) has a clear organization in the azimuthal direction with a dominant peak at $f \approx 320$ Hz ($St = 0.038$) exclusively associated with the axisymmetric (breathing) mode $m = 0$. The secondary peak at $f \approx 1$ kHz ($St = 0.12$) is then shown in figure 15(*b*) to be linked to the first ($m = 1$) Fourier mode. The emerging picture is that of a separation shock characterized by a low-frequency piston-like motion coupled with excitation from the off-axis mode at intermediate frequencies. Moving downstream to $x/r_t = 14.4$, the contribution of the breathing mode at low frequencies becomes less significant, whereas the peak located at $f \approx 1$ kHz ($St \approx 0.12$) for $m = 1$ still persists, suggesting the presence of helical/flapping modes in the separated shear layer, also highlighted by the dominant $m = 1$ dynamics of the high-frequency fluctuations. This observation provides additional support to the screech-like nature of the intermediate peak frequency, since previous experimental and theoretical analyses have shown that at high fully adapted Mach numbers ($M_j > 1.3$) the helical instability wave mode has larger total growth at frequencies close to the screech tone

Downloaded from https://www.cambridge.org/core. IP address: 151.24.234.247, on 27 May 2020 at 05:31:14, subject to the Cambridge Core terms of use, available at https://www.cambridge.org/core/terms. https://doi.org/10.1017/jfm.2020.280

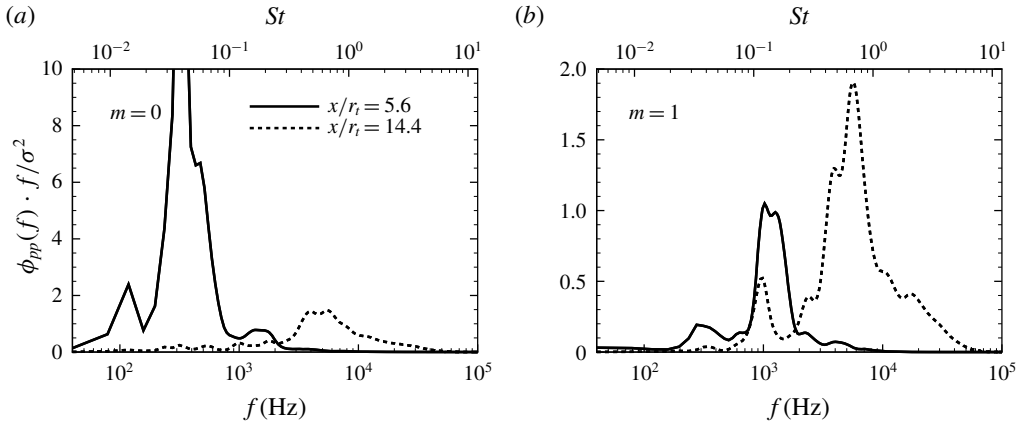

FIGURE 15. Premultiplied spectra of the (*a*) zeroth and (*b*) first Fourier azimuthal mode at two axial locations.

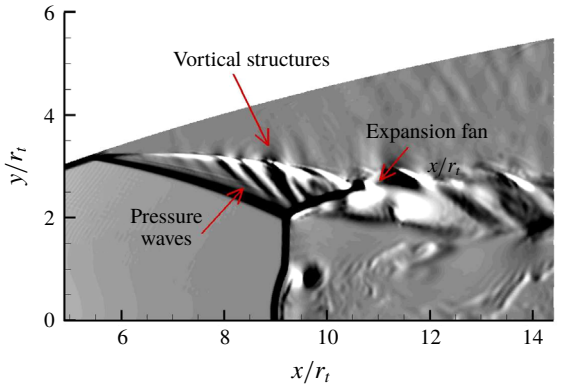

FIGURE 16. Contour of $\partial\rho/\partial x$ from the TIC nozzle flow simulation showing pressure waves radiating from vortical structures in the separated shear layers.

(Tam 1995; Seiner, Manning & Ponton 1987). As previously observed in the spectra at this location ($x/r_t = 14.4$) in figure 10(*c*), most of the energy is a manifestation of high-frequency activity spread over a broad range of azimuthal modes thereby reflecting the turbulent character of the wall-pressure fluctuations in this subsonic recirculation region.

6. Annular supersonic shear layer and Mach disk region

Instantaneous snapshots of the simulated flow are now scrutinized to assess the existence and evolution of coherent vortices along the detached shear layer. Beginning with figure 16, the streamwise derivative of the density field, $\partial\rho/\partial x$, is illustrated for the upstream regions of the separated shear layer where black and white contrasts correspond to compressions (or shocks) and expansions of the gas, respectively. Apparent from this illustration is the formation of coherent vortices that interact with both the separation and reflected shocks. These vortices form at the beginning of the shear layer and are highlighted by the presence of pressure waves extending towards

Downloaded from https://www.cambridge.org/core. IP address: 151.24.234.247, on 27 May 2020 at 05:31:14, subject to the Cambridge Core terms of use, available at https://www.cambridge.org/core/terms. https://doi.org/10.1017/jfm.2020.280

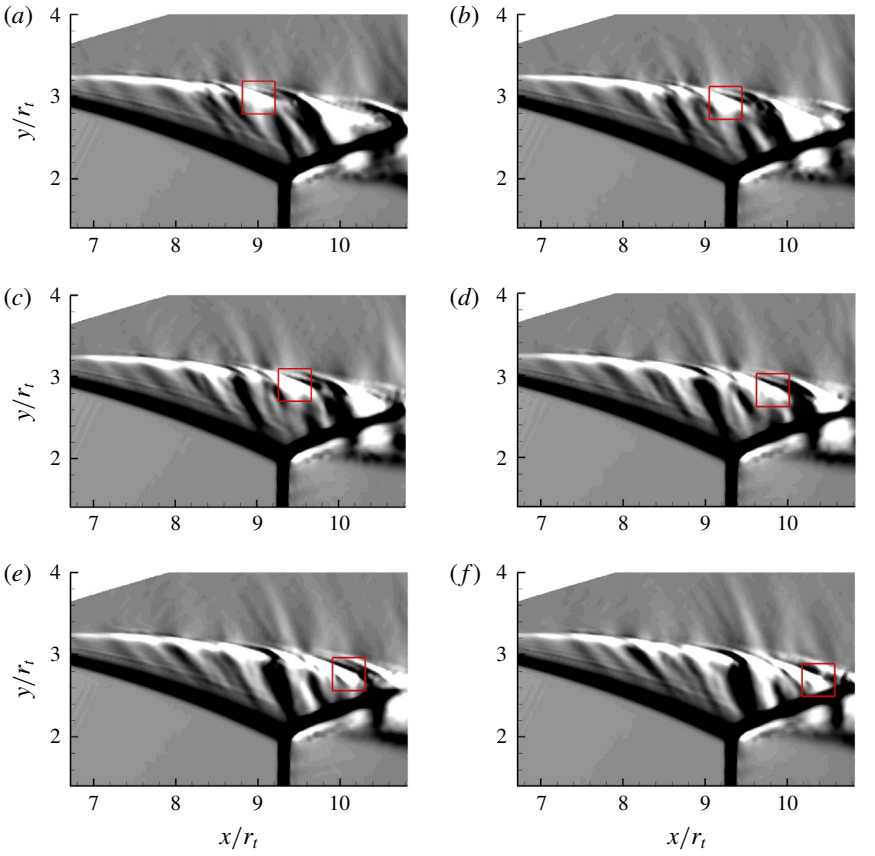

FIGURE 17. Convection of coherent structures in the separated shear layer, shown by means of contours of $\partial\rho/\partial x$. Instantaneous snapshots $\Delta t = 1.3 \times 10^{-5}$ s apart from left to right.

the core of the nozzle where the flow is supersonic. The latter of these shocks is reflected as an expansion fan as it interacts with the upper boundary of the annular shear layer. A close inspection of the evolution of these shear-layer structures is then tracked in figure 17 using a sequence of snapshots of the streamwise component of the density gradient. The eddies comprise elliptical-shaped patterns that remain, for the most part, unchanged and without merging with neighbouring structures, until they interact with the reflected shock. These observations are complementary to those reported by Simon *et al.* (2007) in their analysis of vortex dynamics in a compressible shear layer past an axisymmetric trailing edge. Simon *et al.* (2007) reported instances of merging between vortices, but without the well-known rotational pairing that contributes to the growth rate of subsonic shear layers.

A spectral characterization of the static pressure within the shear layer is now examined using six probe locations, denoted by P_1–P_6 in figure 18(*a*). The power spectral densities of the six time series are shown in figure 18(*b*,*c*). The first four probes are located before the interaction of the reflected shock with the shear layer, whereas the last two probes are placed downstream of this interaction. The signal from probe P_1 is characterized by a small peak centred around 320 Hz ($St = 0.038$), which is clearly linked to the shock movement. The second high-frequency and

Downloaded from https://www.cambridge.org/core. IP address: 151.24.234.247, on 27 May 2020 at 05:31:14, subject to the Cambridge Core terms of use, available at https://www.cambridge.org/core/terms.
https://doi.org/10.1017/jfm.2020.280

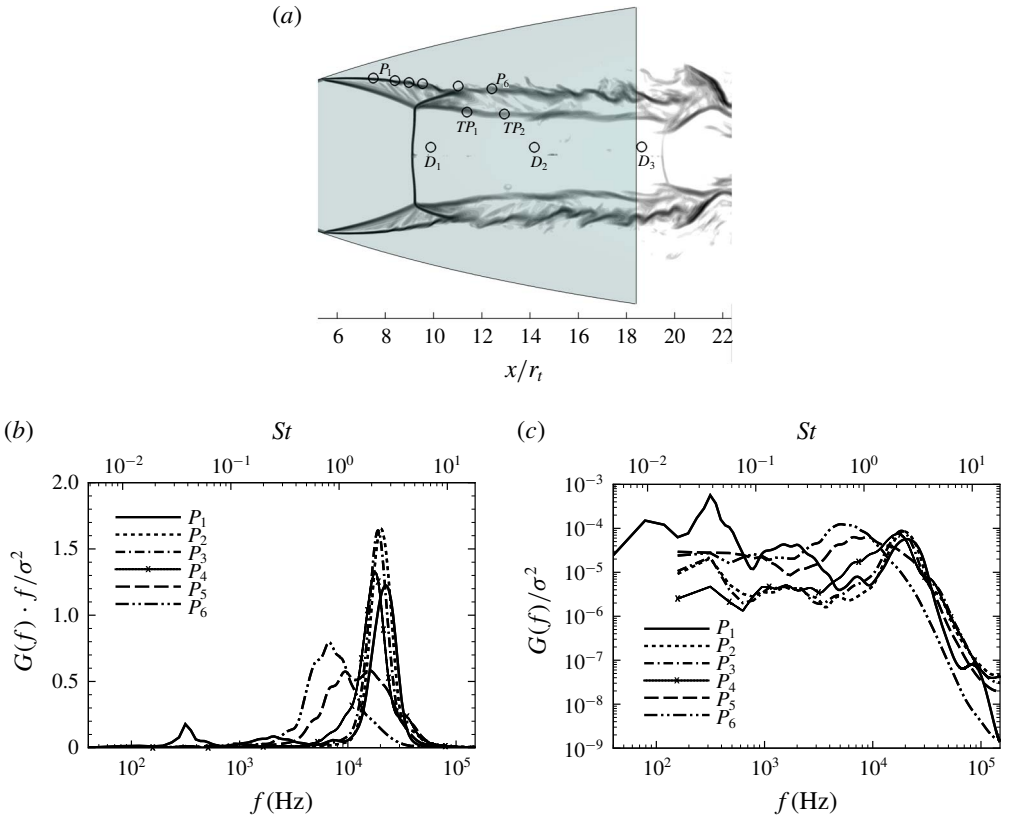

FIGURE 18. (*a*) Positions of the numerical pressure probes. (*b*,*c*) Pressure spectra along the separated shear layer (from P_1 to P_6).

high-energy broad peak is centred around 20 kHz ($S_t = 2.41$) and corresponds to the signature of the dominant shear-layer instability, a feature also visible in the spectra at the downstream probes. From the numerical schlieren images (e.g. figure 17) it is also evident that acoustic disturbances from the region spanned by P_1–P_3 propagate towards the nozzle wall. This is coupled to the spectra imprint on the wall around 10–20 kHz and starting from $x_{r_t} \approx 12$, as was described in the discussion of figure 9. Moving to P_5 and P_6 in figure 18(*b*,*c*), it is observed that the high-frequency component spreads to lower frequencies while the spectral peaks broaden due to the growth of the turbulent structures in the developing shear layer. The contribution of the 320 Hz low-frequency peak reduces moving in the downstream direction and the spectra appear relatively flat in the low-/intermediate-frequency range. This behaviour is consistent with a screech-like scenario where the mixing layer may represent the first path for the downstream propagation of disturbances.

Downstream of the Mach disk, the flow is characterized by intense vortex shedding activity and consequent production of vorticity, as highlighted by the sequence of snapshots of $\partial\rho/\partial x$ reported in figure 19. In figure 19(*a*), the Mach disk is bent upstream while two counter-rotating vortices are emitted. According to Nasuti & Onofri (2009), the bending of the Mach disk is caused by two factors. Foremost, the Mach number field upstream of the shock region is not uniform, especially in the radial direction, as is clearly shown in figure 5. Therefore, in order for the flow

Downloaded from https://www.cambridge.org/core. IP address: 151.24.234.247, on 27 May 2020 at 05:31:14, subject to the Cambridge Core terms of use, available at https://www.cambridge.org/core/terms. https://doi.org/10.1017/jfm.2020.280

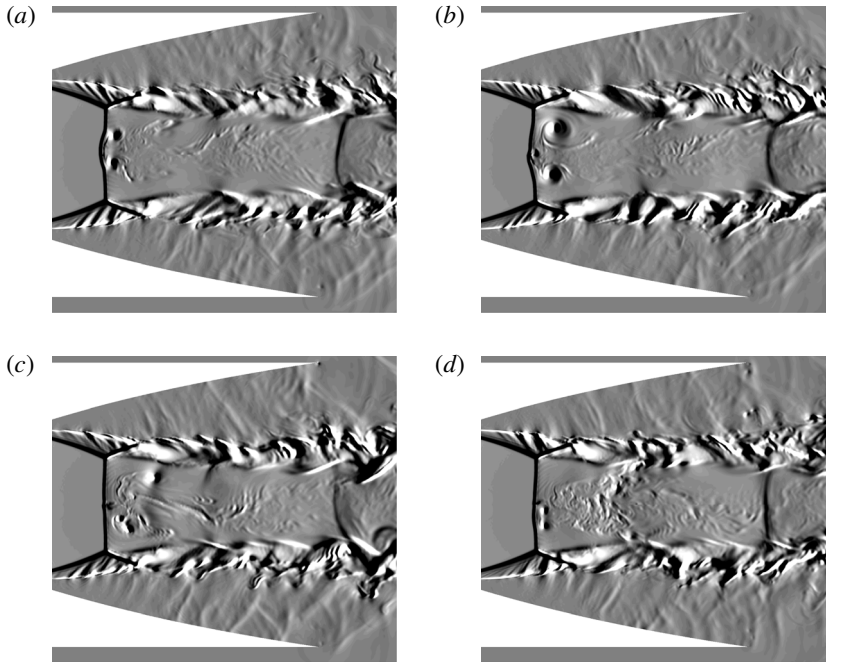

FIGURE 19. Contours of $\partial\rho/\partial x$ showing convection of coherent structures downstream of the Mach disk. Instantaneous snapshots at (*a*) $t = 3.36 \times 10^{-2}$ s, (*b*) $t = 3.39 \times 10^{-2}$ s, (*c*) $t = 3.43 \times 10^{-2}$ s and (*d*) $t = 3.46 \times 10^{-2}$ s.

to adapt to the new static pressure in the subsonic flow after the Mach disk (which is nearly uniform in a time- and space-average sense) the shock has to adjust its curvature radially in order to change intensity. Secondly, the flow unsteadiness causes a continuous variation in the static pressure behind the shock, which causes the Mach disk to oscillate and its curvature to vary. The change in shock intensity along the radial direction causes an entropy gradient downstream and, as described by the Crocco theorem (Crocco 1937), vorticity to be produced. These vortical structures then convect downstream and impinge on both the annular supersonic shear layer and the second shock cell, in a non-symmetric way. In the last snapshot in figure 19(*d*), $t = 3.46 \times 10^{-2}$ s, two new counter-rotating vortices have formed, but are now located below the centreline of the nozzle, thus indicating the non-symmetric behaviour of this shedding phenomenon. An inspection of the flow field along the simulation time also reveals that this activity is not continuous but rather intermittent, as clearly highlighted by the accompanying movie available online at https://doi.org/10.1017/jfm.2020.280.

To further investigate the dynamics of the simulated flow, several additional probes have been placed downstream of the Mach disk (near the nozzle axis) and in the inner shear layer that originates from the triple point of the separation shock reflection, as shown by figure 18(*a*). Figure 20(*a*) shows the premultiplied spectra of the static pressure downstream of the Mach disk. The signal from the first probe (D_1) is characterized by a very broad bump, with the highest peak residing at 905 Hz ($St = 0.11$). The energy associated with this peak originates from unsteady motions of the Mach disk, whose energy decreases rapidly downstream, as shown by the spectra at D_2 and D_3. The internal vortices shed by the Mach disk radiate pressure waves as they convect, stretch and break apart into smaller scales, which explains the broad

Downloaded from https://www.cambridge.org/core. IP address: 151.24.234.247, on 27 May 2020 at 05:31:14, subject to the Cambridge Core terms of use, available at https://www.cambridge.org/core/terms. https://doi.org/10.1017/jfm.2020.280

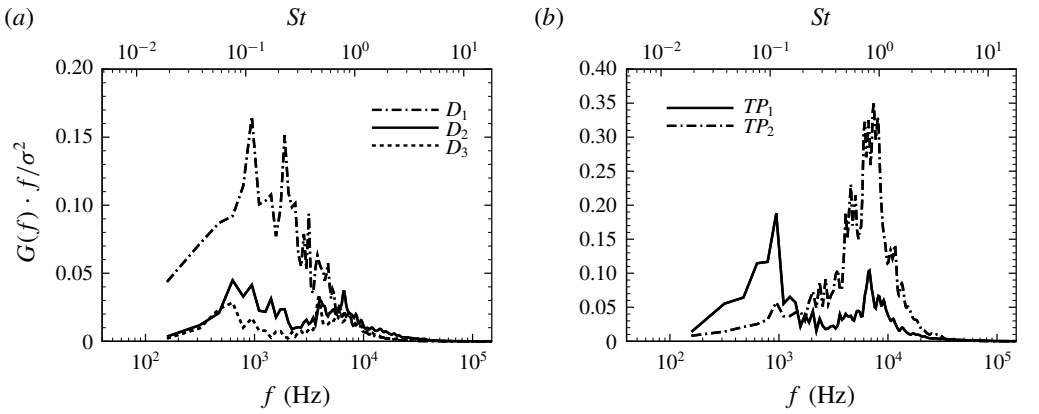

FIGURE 20. Premultiplied frequency spectra of the pressure signal downstream of the Mach disk (*a*) from D_1 to D_3 and (*b*) along the internal shear layer past the triple point (TP_1 and TP_2).

shape in the spectra. Concerning the probe at TP_1, located in the initial part of the inner shear layer (see figure 18*a*), the spectrum reported in figure 20(*b*) reveals the presence of a dominant peak in the intermediate range ($St = 0.11$), with significant energy at the resonant frequency of 1 kHz, associated with the first Fourier-azimuthal mode (see the discussion in § 5). Moving downstream (probe TP_2), the relative importance of the intermediate peak reduces due to the development of the turbulent shear layer, highlighted by a broad peak around 7 kHz ($St = 0.843$).

To characterize the spatial development of the turbulent structures in the core and inner shear-layer regions of this TIC nozzle flow, a global value of the convection velocity has been computed according to (5.10), using the velocity signals taken along a series of probes shown in figure 21(*a*), ranging from the Mach disk up to the second shock. The distribution of C_u is reported in figure 21(*b*) as a function of the streamwise coordinate of the probes. In this region, the flow is characterized by strong accelerations and so it is not surprising to see variations in the convection velocity ranging from a minimum value of $C_u = 0.3u_j$ upstream at $x/r_t = 10.2$ to a maximum value of $C_u \approx u_j$ downstream. If the total time $T_{s,1}$ needed by a turbulent structure to cover the distance between the Mach disk and the second normal shock ($L_{s,1}$) is computed by integrating the distribution of $C_u(x)$ along the streamwise direction, then an average value of the convection velocity for the downstream-propagating disturbances is found to be $\overline{C}_u = L_{s,1}/T_{s,1} = 0.72\,u_j$.

7. Aeroacoustic feedback loop mechanism

It has been shown that the wall-pressure signatures are characterized by the presence of a peak at an intermediate frequency around $f \approx 1$ kHz ($St \approx 0.12$), which is visible both at the shock location and in the downstream region of the nozzle wall where the developing shear layer resides. It has also been shown how this intermediate frequency agrees with the correlation proposed by Tam *et al.* (1986) and is associated with the first Fourier-azimuthal mode ($m = 1$), which happens to be the only mode contributing to the generation of off-axis side loads. Similar results were also observed in the experiments of Jaunet *et al.* (2017). In that, screech tones were not observed in the external ambient field and the existence was postulated of a screech-like mechanism

Downloaded from https://www.cambridge.org/core. IP address: 151.24.234.247, on 27 May 2020 at 05:31:14, subject to the Cambridge Core terms of use, available at https://www.cambridge.org/core/terms.
https://doi.org/10.1017/jfm.2020.280

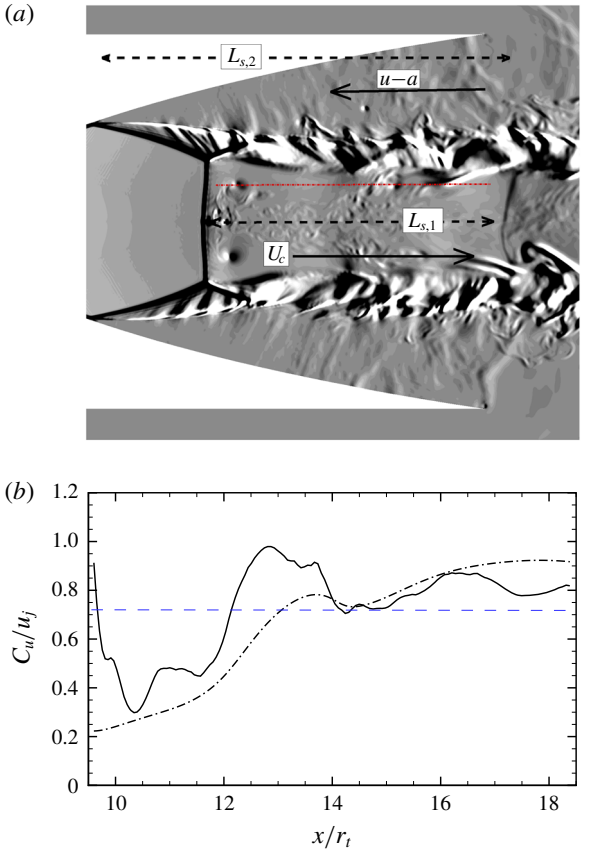

FIGURE 21. (*a*) Visualization of the proposed feedback loop in the shock cell within the nozzle. The horizontal red line denotes the position of the probes for the computation of the convection velocity. (*b*) Distribution of the convection velocity C_u (solid line) as a function of the streamwise coordinate in the core/inner shear-layer region. The distribution of the mean velocity (dash-dotted line) is also given for reference. The horizontal dashed line denotes the average value $\overline{C}_u = 0.72u_j$.

inside the nozzle that was sustained by the presence of the internal subsonic flow region downstream of the Mach disk as the pathway for upstream-propagating waves. The numerical findings from the current DDES model support the existence of an internal feedback loop.

To show that this is the case, the screech model of Powell (1953) is explored, which describes the temporal period of the screech tone as being equal to the time taken by a flow disturbance to propagate downstream by one shock cell plus the time required by an acoustic wave outside the jet to propagate back towards the nozzle lip by the same distance. Following this model, we propose a path for the feedback loop as shown in figure 21. Here, a vortical structure ejected from the Mach disk and triple point translates by a distance $L_{s,1} = 2.38D_j$ (0.176 m) before interacting with the second shock. The interaction perturbs the shock and causes an acoustic wave to be emitted. Since the flow upstream of the second shock is supersonic, the acoustic disturbance can travel upstream, with velocity $u - a$, only through the turbulent recirculating zone external to the annular supersonic shear layer and adjacent to the

Downloaded from https://www.cambridge.org/core. IP address: 151.24.234.247, on 27 May 2020 at 05:31:14, subject to the Cambridge Core terms of use, available at https://www.cambridge.org/core/terms. https://doi.org/10.1017/jfm.2020.280

nozzle wall. This path involves the length $L_{s,2} = 3.35D_j$ (0.247 m) between the second shock and the separation line. Once the acoustic wave reaches the separation line, the oblique shock is perturbed and a new instability wave is emitted in the external annular detached shear layer. Shock foot perturbations propagate in the supersonic detached jet along the oblique shock, reaching the triple point, the internal annular shear layer and the Mach disk. A characteristic time can be evaluated considering the length of the oblique shock $L_{os} = 0.98D_j$ (0.072 m) and a propagation speed equal to $a_{dj} + v_{os}$, where $a_{dj} = 0.35u_j$ is an average speed of sound in the detached jet and $v_{os} = 0.99u_j$ is the average velocity component parallel to the oblique shock. Therefore, as a first approximation, the total period of the loop, T_{sc}, can be modelled by taking into account the distance $L_{s,1}$ for the convective downstream movement, the distance $L_{s,2}$ for the acoustic upstream movement and the distance L_{os}:

$$T_{sc} = \frac{L_{s,1}}{\overline{C}_u} + \frac{L_{s,2}}{|u - a|} + \frac{L_{os}}{|a_{dj} + v_{os}|}$$

resulting in a screech frequency f_{sc}:

$$f_{sc} = \frac{\overline{C}_u}{L_{s,1} + L_{s,2}\dfrac{\overline{C}_u}{|u - a|} + L_{os}\dfrac{\overline{C}_u}{|a_{dj} + v_{os}|}}.$$

Considering a speed of sound in the subsonic separated region $a = 345$ m s^{-1}, an average value of the back flow in the upstream path $u = -80$ m s^{-1} and a convective velocity $\overline{C}_u = 0.72u_j$, the screech frequency is valued at $f_{sc} = 940$ Hz. This value is close to the intermediate peak frequency of $f \approx 1$ kHz, as predicted by the model.

8. Conclusions

A DDES of an overexpanded TIC nozzle flow that features FSS was carried out. The aim of the effort was to identify the driving mechanisms that govern the self-sustained shock motions leading to unsteady wall pressures and ultimately off-axis side loads that form during startup of large-area-ratio nozzles. For these kinds of nozzles, the shock system that forms during overexpanded states causes the flow to separate from the nozzle wall, and occurs well inside the nozzle in regions that are not easily accessible with conventional experimental instruments. Thus the DDES model developed here was proven to be a necessary resource for investigating the flow dynamics associated with a real engineering system under relevant operating conditions (Reynolds number $Re = 1.7 \times 10^7$, NPR = 30.35). The accuracy of the model was validated using laboratory measurements of the static and dynamic wall pressure of the same TIC nozzle contour and operating pressure ratio performed at the University of Texas at Austin.

Analysis of the unsteady wall pressure, comprising Fourier transforms in time and azimuth, identified the wavenumber–frequency makeup of the signatures produced by the shock system and wall-separated flow. Wall-pressure spectra of the dominant azimuthal mode ($m = 0$) at the separation point were shown to be characterized by a peak at $f \approx 320$ Hz ($St \approx 0.038$), implying a low-frequency breathing (piston-like) motion of the shock system. It was postulated that this breathing mode is driven by an acoustic resonance, since its peak frequency falls on the frequency associated with a one-quarter standing wave that forms between the nozzle lip and the separation

Downloaded from https://www.cambridge.org/core. IP address: 151.24.234.247, on 27 May 2020 at 05:31:14, subject to the Cambridge Core terms of use, available at https://www.cambridge.org/core/terms.
https://doi.org/10.1017/jfm.2020.280

shock foot. A secondary peak, at intermediate frequencies around $f \approx 1$ kHz ($St = 0.12$), was also observed and is associated with the first azimuthal mode ($m = 1$); this mode is responsible for the off-axis side loads that act on the nozzle wall and was also found to persist at the same frequency in the wall-pressure spectra of the turbulent entrainment region. The characteristic frequency ($f \approx 1$ kHz) of this phenomenon agrees with the screech model described by Tam *et al.* (1986), suggesting the presence of a feedback loop inside the TIC nozzle with features similar to that observed in overexpanded external jets. Motivated by this observation, a feedback-loop model was proposed that identifies the physical driving mechanisms in high-area-ratio supersonic nozzle flows characterized by the FSS pattern. The loop starts with the turbulent structures in the detached shear layer and past the triple point, along with the intermittent vortex shedding activity of the Mach disk occurring at a frequency of $f \approx 1$ kHz. These vortices meander along the streamwise direction before eventually interacting with the second shock cell at which point acoustic waves are emitted, which propagate upstream through the outer subsonic regions of the flow inside the nozzle wall. The acoustic waves then trigger the birth of new shear-layer instabilities and unsteady shock motions, thereby closing the loop. The findings from this experimentally validated DDES model thus provide support to the speculation recently made by Jaunet *et al.* (2017) on the importance of the internal subsonic region in the feedback loop and underline the key role of both the annular shear layer and the vortex shedding activity of the Mach disk.

Acknowledgements

M.B. was supported by the Scientific Independence of Young Researchers programme 2014 (Active Control of Shock-Wave/Boundary-Layer Interactions project, grant RBSI14TKWU), which is funded by the Ministero Istruzione Università e Ricerca. The authors are especially grateful for the computational resources provided by the Cineca Italian Computing Center under the Italian Super Computing Resource Allocation initiative (ISCRA B/DDES-TIC/HP10BZR88R) and to J. Valdez for his assistance with the experimental campaign.

Declaration of interests

The authors report no conflict of interest.

Supplementary movie

Supplementary movie is available at https://doi.org/10.1017/jfm.2020.280.

REFERENCES

DEL ÁLAMO, J. C. & JIMÉNEZ, J. 2009 Estimation of turbulent convection velocities and corrections to Taylor's approximation. *J. Fluid Mech.* **640**, 5–26.

BAARS, W. J., RUF, J. H. & TINNEY, C. E. 2015 Non-stationary shock motion unsteadiness in an axisymmetric geometry with pressure gradient. *Exp. Fluids* **56**, 92.

BAARS, W. J. & TINNEY, C. E. 2013 Transient wall pressures in an overexpanded and large area ratio nozzle. *Exp. Fluids* **54**, 1468.

BAARS, W. J., TINNEY, C. E., WOCHNER, M. S. & HAMILTON, M. F. 2014 On cumulative nonlinear acoustic waveform distortions from high-speed jets. *J. Fluid Mech.* **749**, 331–366.

Downloaded from https://www.cambridge.org/core. IP address: 151.24.234.247, on 27 May 2020 at 05:31:14, subject to the Cambridge Core terms of use, available at https://www.cambridge.org/core/terms. https://doi.org/10.1017/jfm.2020.280

BAARS, W. J., TINNEY, C. E., RUF, J. H., BROWN, A. M. & MCDANIELS, D. M. 2012 Wall pressure unsteadiness and side loads in overexpanded rocket nozzles. *AIAA J.* **50** (1), 61–73.

BERNARDINI, M. & PIROZZOLI, S. 2009 A general strategy for the optimization of Runge–Kutta schemes for wave propagation phenomena. *J. Comput. Phys.* **228**, 4182–4199.

BERNARDINI, M. & PIROZZOLI, S. 2011 Wall pressure fluctuations beneath supersonic turbulent boundary layers. *Phys. Fluids* **23** (8), 085102.

CANCHERO, A., TINNEY, C. E., MURRAY, N. & RUF, J. H. 2016 Flow and acoustics of clustered rockets during startup. *AIAA J.* **54**, 1660–1669.

CHEN, C. L., CHAKRAVARTHY, S. R. & HUNG, C. M. 1994 Numerical investigation of separated nozzle flows. *AIAA J.* **32** (9), 1836–1843.

CLEMENS, N. T. & NARAYANASWAMY, V. 2014 Low-frequency unsteadiness of shock wave/turbulent boundary layer interactions. *Annu. Rev. Fluid Mech.* **46**, 469–492.

CROCCO, L. 1937 Eine neue Stromfunktion für die Erforschung der Bewegung der Gase mit Rotation. *Z. Angew. Math. Mech.* **17**, 1–7.

DECK, S. 2009 Delayed detached eddy simulation of the end-effect regime and side-loads in an overexpanded nozzle flow. *Shock Waves* **19** (3), 239–249.

DECK, S. 2012 Recent improvements in the zonal detached eddy simulation (ZDES) formulation. *Theor. Comput. Fluid Dyn.* **26** (6), 523–550.

DECK, S. & GUILLEN, P. 2002 Numerical simulation of side loads in an ideal truncated nozzle. *J. Propul. Power* **18** (2), 261–269.

DECK, S. & NGUYEN, A. T. 2004 Unsteady side loads in a thrust-optimized contour nozzle at hysteresis regime. *AIAA J.* **42** (9), 1878–1888.

DOLLING, D. S. & OR, C. T. 1985 Unsteadiness of the shock wave structure in attached and separated compression ramp flows. *Exp. Fluids* **3** (1), 24–32.

DONALD, B. W., BAARS, W. J., TINNEY, C. E. & RUF, J. H. 2014 Sound produced by large area-ratio nozzles during fixed and transient operations. *AIAA J.* **52** (7), 1474–1485.

DUCROS, F., FERRAND, V., NICOUD, F., DARRACQ, D., GACHERIEU, C. & POINSOT, T. 1999 Large-eddy simulation of the shock/turbulence interaction. *J. Comput. Phys.* **152**, 5172013549.

DUMNOV, G. 1996 Unsteady side-loads acting on the nozzle with developed separation zone. In *32nd Joint Propulsion Conference and Exhibit. AIAA Paper* 1996-3220.

DUPONT, P., HADDAD, C. & DEBIÈVE, J. F. 2006 Space and time organization in a shock-induced separated boundary layer. *J. Fluid Mech.* **559**, 255.

EDGINGTON-MITCHELL, D. 2019 Aeroacoustic resonance and self-excitation in screeching and impinging supersonic jets — a review. *Intl J. Aeroacoust.* **18**, 118–188.

ESTRUCH-SAMPER, D. & CHANDOLA, G. 2018 Separated shear layer effect on shock-wave/turbulent-boundary-layer interaction unsteadiness. *J. Fluid Mech.* **848**, 154–192.

FREY, M. & HAGEMANN, G. 2000 Restricted shock separation in rocket nozzles. *J. Propul. Power* **16** (3), 478–484.

HADJADJ, A. & ONOFRI, M. 2009 Nozzle flow separation. *Shock Waves* **19**, 163–169.

HAERING, S, OLIVER, T. & MOSER, R. D. 2019 Towards a predictive hybrid RANS/LES framework. In *AIAA Scitech 2019 Forum. AIAA Paper* 2019-0087.

HAGEMANN, G., FREY, M. & KOSCHEL, W. 2002 Appearance of restricted shock separation in rocket nozzles. *J. Propul. Power* **18** (3), 577–584.

HUNT, J. C. R., WRAY, A. A. & MOIN, P. 1988 Eddies, streams, and convergence zones in turbulent flows. *Proceedings of the 1988 CTR Summer Program N89-24555*. Stanford University.

JAUNET, V., ARBOS, S., LEHNASCH, G. & GIRARD, S. 2017 Wall pressure and external velocity field relation in overexpanded supersonic jets. *AIAA J.* **55** (12), 4245–4257.

KONNO, K. & OHMACHI, T. 1998 Ground-motion characteristics estimated from spectral ratio between horizontal and vertical components of microtremor. *Bull. Seismol. Soc. Am.* **88** (1), 228–241.

LARUSSON, R., ANDERSSON, N. & OSTLUND, J. 2016 Hybrid RANS-LES simulation of separated nozzle flow. In *52nd AIAA/SAE/ASEE Joint Propulsion Conference. AIAA Paper* 2016-4670.

MARTELLI, E., CIOTTOLI, P. P., BERNARDINI, M., NASUTI, F. & VALORANI, M. 2017 Detached eddy simulation of shock unsteadiness in an over-expanded planar nozzle. *AIAA J.* **55** (6), 2016–2028.

Downloaded from https://www.cambridge.org/core. IP address: 151.24.234.247, on 27 May 2020 at 05:31:14, subject to the Cambridge Core terms of use, available at https://www.cambridge.org/core/terms. https://doi.org/10.1017/jfm.2020.280

MARTELLI, E., CIOTTOLI, P. P., SACCOCCIO, L., NASUTI, F., VALORANI, M. & BERNARDINI, M. 2019 Characterization of unsteadiness in an overexpanded planar nozzle. *AIAA J.* **57** (1), 239–251.

MEMMOLO, A., BERNARDINI, M. & PIROZZOLI, S. 2018 Scrutiny of buffet mechanisms in transonic flow. *Intl J. Numer. Meth. Heat Fluid Flow* **28**, 1031–1046.

NASUTI, F. & ONOFRI, M. 1998 Viscous and inviscid vortex generation during start-up of rocket nozzles. *AIAA J.* **36** (5), 809–815.

NASUTI, F. & ONOFRI, M. 2009 Shock structure in separated nozzle flows. *Shock Waves* **19** (3), 229–237.

NAVE, L. H. & COFFEY, G. A. 1973 Sea level side loads in high-area-ratio rocket engines. In *9th Propulsion Conference. AIAA Paper* 1973-1284.

NGUYEN, A. T., DENIAU, H., GIRARD, S. & ALZIARY DE ROQUEFORT, T. 2003 Unsteadiness of flow separation and end-effects regime in a thrust-optimized contour rocket nozzle. *Flow Turbul. Combust.* **71** (1), 161–181.

OSTLUND, J. 2002 Flow process in rocket engine nozzles with focus on flow separation and side-loads. PhD Thesis, Royal Inst. of Tech., Stockhom, TRITA-MEK.

PACK, D. C. 1950 A note on Prandtl's formula for the wave-length of a supersonic gas jet. *Q. J. Mech. Appl. Maths* **3**, 173–181.

PIROZZOLI, S. 2011 Numerical methods for high-speed flows. *Annu. Rev. Fluid Mech.* **43**, 163–194.

PIROZZOLI, S., BERNARDINI, M. & GRASSO, F. 2008 Characterization of coherent vortical structures in a supersonic turbulent boundary layer. *J. Fluid Mech.* **613**, 205–231.

POWELL, A. 1953 On the mechanism of choked jet noise. *Proc. Phys. Soc. Sect.* B **66** (12), 1039–1056.

RAMAN, G. 1999 Supersonic jet screech: half-century from powell to the present. *J. Sound Vib.* **225** (3), 543–571.

RAO, G. V. R. 1958 Exhaust nozzle contour for optimum thrust. *Jet Propul.* **28** (6), 377–382.

RENARD, N. & DECK, S. 2015 On the scale-dependent turbulent convection velocity in a spatially developing flat plate turbulent boundary layer at Reynolds number $Re_\theta = 13\,000$. *J. Fluid Mech.* **775**, 105–148.

ROMANO, G. P. 1995 Analysis of two-point velocity measurements in near-wall flows. *Exp. Fluids* **20**, 68–83.

RUF, J., MCDANIELS, D. & BROWN, A. 2010 Details of side load test data and analysis for a truncated ideal contour nozzle and a parabolic contour nozzle. In *46th AIAA/ASME/SAE/ASEE Joint Propulsion Conference & Exhibit. AIAA Paper* 2010-6813.

RUF, J. H., MCDANIELS, D. M. & BROWN, A. M. 2009 Nozzle side load testing and analysis at Marshall Space Flight Center. In *45th AIAA/ASME/SAE/ASEE Joint Propulsion Conference. AIAA Paper* 2009-4856.

SANDHAM, N. D. & REYNOLDS, W. C. 1991 Three-dimensional simulations of large eddies in the compressible mixing layer. *J. Fluid Mech.* **224**, 133–158.

SCHMUCKER, R. H. 1984 Flow process in overexpanded chemical rocket nozzles. Part 2. Side loads due to asymmetric separation. NASA TM-77395.

SEINER, J. M., MANNING, J. C. & PONTON, M. K. 1987 Model and full scale study of twin supersonic plume resonance. In *25th AIAA Aerospace Sciences Meeting. AIAA Paper* 1987-244.

SHAMS, A., LEHNASCH, G., COMTE, P., DENIAU, H. & ALZIARY DE ROQUEFORT, T. 2013 Unsteadiness in shock-induced separated flow with subsequent reattachment of supersonic annular jet. *Comput. Fluids* **78**, 63–74.

SHUR, M. L., SPALART, P. R., STRELETS, M. K. & TRAVIN, A. K. 2015 An enhanced version of DES with rapid transition from RANS to LES in separated flows. *Flow Turbul. Combust.* **95** (4), 709–737.

SIMON, F., DECK, S., GUILLEN, P., SAGAUT, P. & MERLEN, A. 2007 Numerical simulation of the compressible mixing layer past an axisymmetric trailing edge. *J. Fluid Mech.* **591**, 215–253.

Downloaded from https://www.cambridge.org/core. IP address: 151.24.234.247, on 27 May 2020 at 05:31:14, subject to the Cambridge Core terms of use, available at https://www.cambridge.org/core/terms. https://doi.org/10.1017/jfm.2020.280

SPALART, P. R., DECK, S., SHUR, M. L., SQUIRES, K. D., STRELETS, M. K. & TRAVIN, A. K. 2006 A new version of detached-eddy simulation, resistant to ambiguous grid densities. *Theor. Comput. Fluid Dyn.* **20**, 181–195.

SPALART, P. R., JOU, W. H., STRELETS, M. & ALLMARAS, S. R. 1997 Comments on the feasibility of LES for wings, and on a hybrid RANS/LES approach. In *Advances in DNS/LES*, pp. 137–147.

STARK, R. 2013 Flow separation in rocket nozzles – an overview. In *49th AIAA/ASME/SAE/ASEE Joint Propulsion Conference. AIAA Paper* 2013-3840.

TAM, C. K. W. 1995 Supersonic jet noise. *Annu. Rev. Fluid Mech.* **27**, 17–43.

TAM, C. K. W., SEINER, J. M. & YU, J. C. 1986 Proposed relationship between broadband shock associated noise and screech tones. *J. Sound Vib.* **110** (2), 309–321.

VERMA, S. B. & HAIDN, O. 2014 Unsteady shock motions in an over-expanded parabolic rocket nozzle. *Aerosp. Sci. Technol.* **39**, 48–71.

WONG, H. Y. W. 2005 Theoretical prediction of resonance in nozzle flows. *J. Propul. Power* **21** (2), 300–313.

ZAMAN, K. B. M. Q., DAHL, M. D., BENCIC, T. J. & LOH, C. Y. 2002 Investigation of a 'transonic resonance' with convergent divergent nozzles. *J. Fluid Mech.* **463**, 313–343.

Downloaded from https://www.cambridge.org/core. IP address: 151.24.234.247, on 27 May 2020 at 05:31:14, subject to the Cambridge Core terms of use, available at https://www.cambridge.org/core/terms. https://doi.org/10.1017/jfm.2020.280